Structural and Multidisciplinary Optimization (2020) 62:3205–3227
https://doi.org/10.1007/s00158-020-02671-8

RESEARCH PAPER

Topology optimization considering the Drucker–Prager criterion with a surrogate nonlinear elastic constitutive model

Tuo Zhao[1] · Eduardo N. Lages[2] · Adeildo S. Ramos Jr[2] · Glaucio H. Paulino[1]

Received: 17 January 2019 / Revised: 19 June 2020 / Accepted: 24 June 2020 / Published online: 29 October 2020

Abstract

We address material nonlinear topology optimization problems considering the Drucker–Prager strength criterion by means of a surrogate nonlinear elastic model. The nonlinear material model is based on a generalized J_2 deformation theory of plasticity. From an algorithmic viewpoint, we consider the topology optimization problem subjected to prescribed energy, which leads to robust convergence in nonlinear problems. The objective function of the optimization problem consists of maximizing the strain energy of the system in equilibrium subjected to a volume constraint. The sensitivity analysis is quite effective and efficient in the sense that there is no extra adjoint equation. In addition, the nonlinear structural equilibrium problem is solved through direct minimization of the structural strain energy using Newton's method with an inexact line search strategy. Four numerical examples demonstrate features of the proposed nonlinear topology optimization framework considering the Drucker–Prager strength criterion.

Keywords Nonlinear topology optimization · Drucker–Prager strength criterion · Elasticity · Surrogate model · ABAQUS UMAT

1 Introduction

Robert Hooke was one of the greatest scientists of the seventeenth century and his discovery of elasticity (he described the finding in the anagram "ceiiinosssttuv," whose solution he later published as "Ut tension, sic vis" which translates to "As the extension, so the force" (Davidson 2010)) had a remarkable influence in the world since then, and continues to impact the world that we live today, including various fields of science and technology (Marsden and Hughes 1983, Holmes 2019, Hooke Public Lecture Series at the Univ. of Oxford 2014). For instance, the use of elastic springs permeates modern technology, from toys to mechanical components in cars and airplanes. In terms of materials, nonlinear elasticity can describe the behavior of soft materials, including elastomers and gels that can undergo large deformations (Marsden and Hughes 1983). Following and building upon Hooke's ubiquitous legacy, we make use of nonlinear elasticity to investigate topologically optimized structures and to compare our results with the existing literature using dissipative models such as elastoplasticity. In essence, we verify numerically that the topologically optimized nonlinear elastic solution (based on deformation theory of plasticity) is equivalent to the plastic solution (based on flow theory of plasticity) under proportional loading.

Naturally, most papers in the literature that investigate topology optimization with the Drucker–Prager elastoplastic materials use a plasticity-based formulation (Swan and Kosaka 1997; Bogomolny and Amir 2012; Alberdi and Khandelwal 2017). However, the role that elastic nonlinearity plays has not been investigated independently in terms of optimal design. *To address this issue, we propose a material nonlinear topology optimization approach using the Drucker–Prager criterion with a surrogate nonlinear elastic constitutive model.* Essentially, we want to verify to which extent a purely elastic

Dedicated to the memory of Robert Hooke (July 28, 1635 – March 3, 1703)

Responsible Editor: Helder C. Rodrigues

Electronic supplementary material The online version of this article (https://doi.org/10.1007/s00158-020-02671-8) contains supplementary material, which is available to authorized users.

✉ Glaucio H. Paulino
paulino@gatech.edu

[1] School of Civil and Environmental Engineering, Georgia Institute of Technology, 790 Atlantic Drive, Atlanta, GA 30332-0355, USA

[2] Center of Technology, Federal University of Alagoas, Maceió, AL, Brazil

theory can reproduce some (or most) of the results in the literature, which are based on plasticity.

We utilize a nested optimization formulation, which consists of maximizing the strain energy of the system in equilibrium subjected to a volume constraint. To solve the nonlinear state equations in the formulation, we use an energy control approach. This approach prescribes a certain value of energy C_0 in all optimization design cycles until the optimal design is reached. The energy control approach is illustrated in Fig. 1 assuming a generalized two degrees of freedom problem (more detailed explanation about this problem is given in Appendix A). When we use the energy control approach, an appropriate prescribed energy C_0 can be chosen which depends on the expected nonlinear behavior. Choosing a value of C_0 can also be considered as a way of controlling when the material model reaches the limit stage.[1] In addition, numerical examples show that the energy control approach leads to robust convergence in solving the nonlinear state equations.

The remainder of this paper is organized as follows. Section 2 details the nonlinear elastic constitutive model. Section 3 presents the optimization formulation and related sensitivity analysis. Section 4 contributes four representative numerical examples. Section 5 presents the conclusions. Six Appendices complement the paper: one demonstrates the energy control approach using a simple truss example; one estimates the limit value of the prescribed energy for a design optimization problem with a fixed volume fraction; one illustrates the relationship between the increment of principal stress on the Drucker–Prager strength surface and the increment of principal strain; one shows how to solve the nonlinear state equations using Newton's method with an inexact line search; one provides the ABAQUS® user subroutine UMAT for the present nonlinear elastic constitutive model considering the Drucker–Prager criterion; and another presents the nomenclature.

2 Equivalent nonlinear elastic constitutive model

The behavior of inelastic materials that exhibit pressure-dependent yielding (e.g., concrete and soils) is characterized by elastic nonlinearity and path-dependency (i.e., physical processes such as energy dissipation and unloading). The commonly used theory to capture the full path-dependent response of plastic materials is the so-called flow theory of plasticity (Hill 1950; Lubliner 1990). Since the overall response is history-dependent, it is determined incrementally by integrating the rate-type constitutive equations along a given path of loading (Lubarda 2000; Souza Neto et al. 2008).

There exists an early theory of plasticity proposed by Hencky (1924), known as the deformation theory of plasticity, in which the constitutive equations are the equations of a nonlinear elastic body under proportional loading (Kachanov 1971). Adopting a generalized J_2 deformation theory (Chen and Han 1988), Sonato et al. (2015) suggested a nonlinear elastic model for deriving the nonlinear transmission conditions of pressure-dependent interphases. They verified that the deformation theory for Drucker–Prager material with linear hardening is equivalent to the flow theory for several monotonic loadings. Here, we explore this deformation theory based nonlinear elastic model for Drucker–Prager materials and integrate it in the context of topology optimization.

The present material nonlinear elastic model is governed by the Drucker–Prager strength criterion. Inspired by Hooke's law (1678) and subsequent developments (Timoshenko 1934), we use a generalized nonlinear elastic constitutive relationship in the following form:

$$\boldsymbol{\sigma} = \lambda J_1(\boldsymbol{\varepsilon})\boldsymbol{I} + 2\mu\boldsymbol{\varepsilon} \tag{1}$$

where $\boldsymbol{I}$ is the second-order identity tensor, $\boldsymbol{\sigma}$ and $\boldsymbol{\varepsilon}$ are the stress and strain tensors, while λ and μ are usual Lame's parameters. However, we assume that both Lame's parameters are functions of two invariants of the strain tensor:

$$\lambda = \lambda(J_1(\boldsymbol{\varepsilon}), J_2(\boldsymbol{\varepsilon}_d)), \mu = \mu(J_1(\boldsymbol{\varepsilon}), J_2(\boldsymbol{\varepsilon}_d)) \tag{2}$$

where the invariants of the strain tensor are defined by:

$$J_1(\boldsymbol{\varepsilon}) = \mathrm{trace}(\boldsymbol{\varepsilon}), J_2(\boldsymbol{\varepsilon}_d) = \frac{1}{2}\boldsymbol{\varepsilon}_d : \boldsymbol{\varepsilon}_d \tag{3}$$

with $\boldsymbol{\varepsilon}_d = \boldsymbol{\varepsilon} - (1/3)\mathrm{trace}(\boldsymbol{\varepsilon})\boldsymbol{I}$, and we denote : as the double tensor contraction operator, as usual. The J_2 deformation theory (Hencky 1924) is generalized to the case of pressure-sensitive materials so that the first invariant J_1 is included in the constitutive model. In this case, the Lame's parameters can be conveniently written as (Sonato et al. 2015):

$$\lambda(\phi_1, \phi_2) = \frac{3\upsilon + (\phi_2 - \phi_1)E}{3(1 + \upsilon + \phi_2 E)(1 - 2\upsilon + \phi_1 E)}E, \tag{4}$$

$$\mu(\phi_2) = \frac{E}{2(1 + \upsilon + \phi_2 E)}$$

respectively, where E is Young's modulus, υ is Poisson's ratio, and ϕ_1 and ϕ_2 are functions which represent the

[1] For several inelastic constitutive models, the energy control has better convergence behavior than the load control method. For instance, Crisfield (1991) pointed out that load control is not preferable when a small addition to the load causes a relatively large additional displacement or when limit points are encountered. The energy control approach overcomes this difficulty in regions where the stress state tends to reach the strength limit.

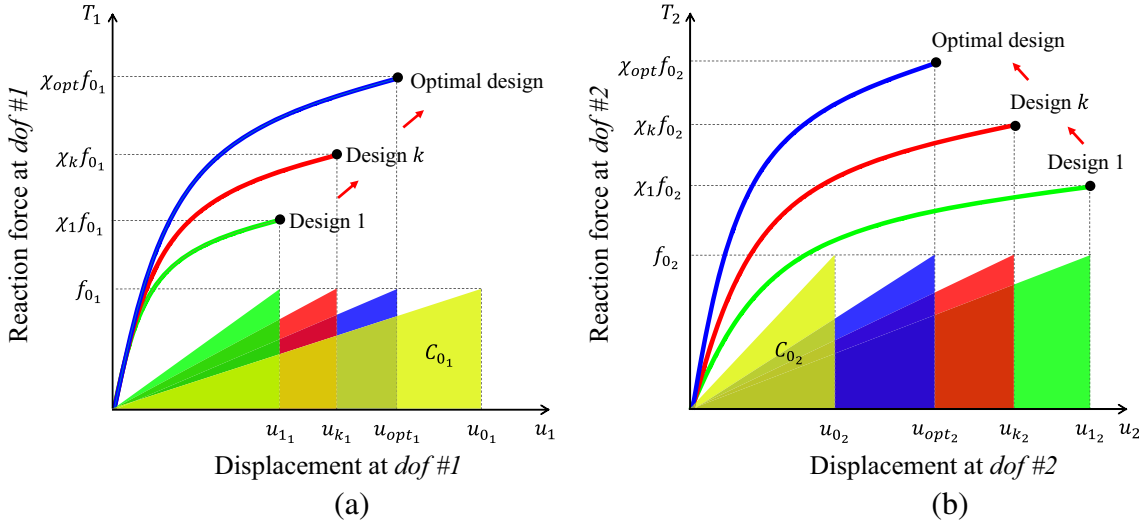

Fig. 1 Illustration of the proposed energy control approach. The approach prescribes a certain value of energy C_0 (i.e., $C_0 = C_{01} + C_{02}$, where C_{01} and C_{02} are the area of the shaded triangles) for all design cycles until the optimal design is obtained. In this example with two degrees of freedom (which generalizes to multi-dof), we assume that two reference forces (i.e., $f_{0_1} < f_{0_2}$) are applied at each of the two dofs, respectively, and that $\chi_k > 1$, which refers to the load factor at the k-th design cycle. **a** and **b** are reaction force (T) versus displacement (u) diagrams for each dof. The shaded area represents the prescribed energy at the initial optimization iteration (yellow), 1st iteration (green), generic k-th iteration (red), and the final optimal design (blue). The sum of the shaded area with the same color is a constant which is the prescribed energy C_0

hardening behavior of the material. In the case of linear elastic loading, $\phi_1 = \phi_2 = 0$, while in the case of nonlinear elastic loading $\phi_1 \neq 0$ and $\phi_2 > 0$. We assume that ϕ_1 and ϕ_2 are functions of the two invariants of the strain tensor, and define ϕ_2 as non-negative, i.e.:

$$\phi_1 = \phi_1(J_1(\boldsymbol{\varepsilon}), J_2(\boldsymbol{\varepsilon}_d)), \quad \phi_2 = \phi_2(J_1(\boldsymbol{\varepsilon}), J_2(\boldsymbol{\varepsilon}_d)) \geq 0 \tag{5}$$

Sonato et al. (2015) obtained the functions ϕ_1 and ϕ_2 considering a material obeying the Drucker–Prager strength criterion (Drucker and Prager 1952) in the following form:

$$f(\boldsymbol{\sigma}) = \beta J_1(\boldsymbol{\sigma}) + \sqrt{J_2(\boldsymbol{s})} - k_s \tag{6}$$

where the first invariant of the stress tensor $J_1(\boldsymbol{\sigma})$ and the second invariant of the deviatoric stress tensor $J_2(\boldsymbol{s})$ are expressed, respectively, as:

$$J_1(\boldsymbol{\sigma}) = \text{trace}(\boldsymbol{\sigma}), \quad J_2(\boldsymbol{s}) = \frac{1}{2}\boldsymbol{s} : \boldsymbol{s} \tag{7}$$

where $\boldsymbol{s} = \boldsymbol{\sigma} - (1/3)\text{trace}(\boldsymbol{\sigma})\boldsymbol{I}$. In (6), β and k_s are assumed to be positive constants for an elastic-perfectly-plastic material in the case of uniaxial stress tests. The two parameters β and k_s are defined as:

$$\beta = \frac{1}{2\sqrt{3}} \frac{(1-2\upsilon^p)}{(1+\upsilon^p)}, \quad k_s = \left(\beta + \frac{1}{\sqrt{3}}\right)\sigma_y \tag{8}$$

where υ^p is the plastic Poisson's ratio and σ_y is the uniaxial strength stress of the material. The function ϕ_1 is derived as:

$$\phi_1(J_1(\boldsymbol{\varepsilon}), J_2(\boldsymbol{\varepsilon}_d)) = \frac{6\beta\{3\beta(1+\upsilon)EJ_1(\boldsymbol{\varepsilon}) + (1-2\upsilon)[3E\sqrt{J_2(\boldsymbol{\varepsilon}_d)} - (3\beta+\sqrt{3})(1+\upsilon)\sigma_y]\}}{E[3E(J_1(\boldsymbol{\varepsilon}) - 6\beta\sqrt{J_2(\boldsymbol{\varepsilon}_d)}) + 6\beta(3\beta+\sqrt{3})(1+\upsilon)\sigma_y]} \tag{9}$$

Similarly, the function ϕ_2 is obtained as:

$$\phi_2(J_1(\boldsymbol{\varepsilon}), J_2(\boldsymbol{\varepsilon}_d)) = \frac{3\beta(1+\upsilon)EJ_1(\boldsymbol{\varepsilon}) + (1-2\upsilon)[3E\sqrt{J_2(\boldsymbol{\varepsilon}_d)} - (3\beta+\sqrt{3})(1+\upsilon)\sigma_y]}{E\{18\beta^2 E\sqrt{J_2(\boldsymbol{\varepsilon}_d)} - 3\beta[EJ_1(\boldsymbol{\varepsilon}) - (1-2\upsilon)\sigma_y] + \sqrt{3}(1-2\upsilon)\sigma_y\}} \tag{10}$$

Note that the function ϕ_2 has two limit states, i.e.:

1. linear elastic limit when the numerator is equal to zero ($\phi_2 = 0$);
2. singular limit as the denominator approaches zero (the singular point at the apex of the Drucker–Prager cone).

Next, we mathematically quantify the two limits, which are essential to define the stress states and the strain energy density function of the constitutive model. For the sake of notation, let us define five constant scalars a, b, c, d, and e as follows:

$$a = 3\beta(1+\upsilon)E, \quad b = 3(1-2\upsilon)E, \quad c = -\left(3\beta+\sqrt{3}\right)(1+\upsilon)(1-2\upsilon)\sigma_y,$$
$$d = -3\beta E^2, \quad e = 18\beta^2 E^2, \quad f = \left(3\beta+\sqrt{3}\right)(1-2\upsilon)E\sigma_y \tag{11}$$

Then, we rewrite (10), in simplified form, as:

$$\phi_2(J_1(\boldsymbol{\varepsilon}), J_2(\boldsymbol{\varepsilon}_d)) = \frac{aJ_1(\boldsymbol{\varepsilon}) + b\sqrt{J_2\left(\boldsymbol{\varepsilon}_d\right)} + c}{dJ_1(\boldsymbol{\varepsilon}) + e\sqrt{J_2\left(\boldsymbol{\varepsilon}_d\right)} + f} \tag{12}$$

Now, we introduce a non-negative scaling factor t and write the strain tensor and the deviatoric strain tensor as follows:

$$\boldsymbol{\varepsilon}^{'} = t\boldsymbol{\varepsilon}, \quad \boldsymbol{\varepsilon}_d^{'} = t\boldsymbol{\varepsilon}_d \tag{13}$$

By substituting (13) into (12), we obtain ϕ_2 as the ratio of two functions, $M(t)$ and $N(t)$, as follows:

$$\phi_2\left(J_1\left(\boldsymbol{\varepsilon}^{'}\right), J_2\left(\boldsymbol{\varepsilon}_d^{'}\right)\right) = \frac{aJ_1(t\boldsymbol{\varepsilon}) + b\sqrt{J_2\left(t\boldsymbol{\varepsilon}_d\right)} + c}{dJ_1(t\boldsymbol{\varepsilon}) + e\sqrt{J_2\left(t\boldsymbol{\varepsilon}_d\right)} + f}$$

$$= \frac{taJ_1(\boldsymbol{\varepsilon}) + tb\sqrt{J_2\left(\boldsymbol{\varepsilon}_d\right)} + c}{tdJ_1(\boldsymbol{\varepsilon}) + te\sqrt{J_2\left(\boldsymbol{\varepsilon}_d\right)} + f} = \frac{M(t)}{N(t)} \tag{14}$$

We obtain the two limit states of function ϕ_2 by defining $M(t)$ and $N(t)$ equal to zero, respectively:

$$\begin{aligned} M\left(t^L\right) = 0 \Rightarrow t^L &= -\frac{c}{aJ_1(\boldsymbol{\varepsilon}) + b\sqrt{J_2\left(\boldsymbol{\varepsilon}_d\right)}} \\ N\left(t^N\right) = 0 \Rightarrow t^N &= -\frac{f}{dJ_1(\boldsymbol{\varepsilon}) + e\sqrt{J_2\left(\boldsymbol{\varepsilon}_d\right)}} \end{aligned} \tag{15}$$

where t^L defines the limit point of linear elastic loading, and t^N is the singular limit point of the function ϕ_2. The function $M(t)$ is always non-negative, while the function $N(t)$ can be either positive or negative, which is related to the scaling factor t, i.e.:

$$\begin{aligned} N(t) > 0 &\Rightarrow t < t^N \\ N(t) < 0 &\Rightarrow \mathrm{t} > t^N \end{aligned} \tag{16}$$

Therefore, the singular state of the function ϕ_2 is expressed as:

$$\lim_{t \to t^{N+}} \phi_2 = \lim_{N \to 0^-} \phi_2 = -\infty \quad \lim_{t \to t^{N-}} \phi_2 = \lim_{N \to 0^+} \phi_2 = \infty \tag{17}$$

We numerically verify that the singular state of ϕ_2 never happens during the numerical simulation of all the examples in this paper. Furthermore, note that the expression of ϕ_2 in (10) is only valid when $\phi_2 \geq 0$ because we define ϕ_2 as non-negative in (5). For any strain state that causes a negative ϕ_2, the corresponed stress state is a constant defined as follows:

$$\boldsymbol{\sigma}^N = \frac{k_s}{3\beta}\boldsymbol{I} \tag{18}$$

We remark that the constant stress state in (18) occurs at the apex of the Drucker–Prager cone, which is commonly observed in the flow theory of plasticity.

We summarize the stress state update scheme for the nonlinear elastic model using the graphical representation of Fig. 2. In the coordinates of stress invariants, the space is divided into three regions based on the function ϕ_2. The corresponding stress states can be updated as follows:

Region #1: linear elastic loading if $f(\boldsymbol{\sigma}^{\mathrm{tr}}) \leq 0$ (i.e., $\phi_1 = \phi_2 = 0$),

$$\boldsymbol{\sigma} = \boldsymbol{\sigma}^{\mathrm{tr}} \in \left[\mathbf{0} \quad \boldsymbol{\sigma}^L\right] \tag{19}$$

where $\boldsymbol{\sigma}^{\mathrm{tr}}$ is the linear elastic trial stress state, and $f(\boldsymbol{\sigma}^{\mathrm{tr}}) \leq 0$ indicates that the current trial stress state is in the linear elastic region. Moreover, $\boldsymbol{\sigma}^L$ is the linear elastic limit of the stress tensor reached in the direction of strain $\boldsymbol{\varepsilon}$.

Region #2: nonlinear elastic loading if $f(\boldsymbol{\sigma}^{\mathrm{tr}}) > 0$ and $\phi_2 > 0$,

$$\boldsymbol{\sigma} = \boldsymbol{\sigma}^{'}(\phi_1, \phi_2) \in \left[\boldsymbol{\sigma}^L \quad \boldsymbol{\sigma}^N\right] \tag{20}$$

where the stress state $\boldsymbol{\sigma}^{'}$ is based on the functions ϕ_1 and ϕ_2. In addition, $\boldsymbol{\sigma}^N$ is the nonlinear elastic limit of the stress tensor reached in the direction of strain $\boldsymbol{\varepsilon}$.

Region #3: apex zone if $f(\boldsymbol{\sigma}^{\mathrm{tr}}) > 0$ and $\phi_2 < 0$,

$$\boldsymbol{\sigma} = \boldsymbol{\sigma}^N \tag{21}$$

and $\boldsymbol{\sigma}^N$ is constant, as defined in (18).

To better illustrate the proposed nonlinear elastic constitutive model, we plot its principal stress state in Fig. 3. In the principal stress coordinates, the yellow cone represents the analytical Drucker–Prager strength surface and the blue dots are the principal stress state generated from the surrogate nonlinear elastic model. Since all the blue dots are located on the surface of the yellow cone, then the proposed constitutive model satisfies the Drucker–Prager strength criterion. In addition, Fig. 4 illustrates the projection of the trial inadmissible linear elastic stress state on the strength surface. The red dots represent the trajectory of the elastic trial stress state, and the blue dots are the projected plastic stress state on the strength surface. The red and blues dots are connected by the green lines, which are parallel and equally spaced. Those green lines

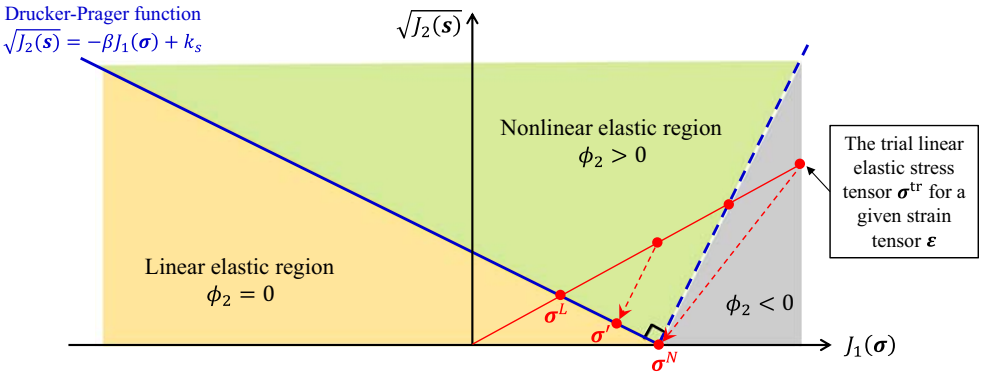

Fig. 2 A graphical representation of the stress state update scheme for the surrogate nonlinear elastic constitutive model

indicate that the increment of the principal stresses on the strength surface is constant with respect to the increment of the principal strain (see Appendix C).

2.1 Analytical strain energy density function φ

The nonlinear elastic constitutive model in (1) can be characterized by the strain energy density function $\varphi(J_1(\boldsymbol{\varepsilon}), J_2(\boldsymbol{\varepsilon}_d))$ such that:

$$\boldsymbol{\sigma} = \frac{\partial \varphi(J_1(\boldsymbol{\varepsilon}), J_2(\boldsymbol{\varepsilon}_d))}{\partial \boldsymbol{\varepsilon}} \tag{22}$$

We revisit the equivalent stress states of Fig. 2 in terms of the corresponding strain energy density function and obtain the expression of $\varphi(J_1(\boldsymbol{\varepsilon}), J_2(\boldsymbol{\varepsilon}_d))$ in three different regions as follows:

Region #1: linear elastic loading if $f(\boldsymbol{\sigma}^{tr}) \le 0$ (i.e., $\phi_1 = \phi_2 = 0$),

$$\boxed{\varphi = \frac{1}{2}\boldsymbol{\sigma}^{tr} : \boldsymbol{\varepsilon}'} \tag{23}$$

Region #2: nonlinear elastic loading if $f(\boldsymbol{\sigma}^{tr}) > 0$ and $\phi_2 > 0$,

$$\varphi = \varphi^L + \int_0^1 \boldsymbol{\sigma}' \left(\boldsymbol{\varepsilon}'(t)\right) dt : \left(\boldsymbol{\varepsilon} - \boldsymbol{\varepsilon}^L\right) \tag{24}$$

where φ^L is the linear elastic strain energy density defined as:

$$\varphi^L = \frac{1}{2}\boldsymbol{\sigma}^L : \boldsymbol{\varepsilon}^L \tag{25}$$

and $\boldsymbol{\sigma}^L$ and $\boldsymbol{\varepsilon}^L$ are, respectively, the linear elastic limit of the stress and strain tensor reached in the direction of strain $\boldsymbol{\varepsilon}$. In

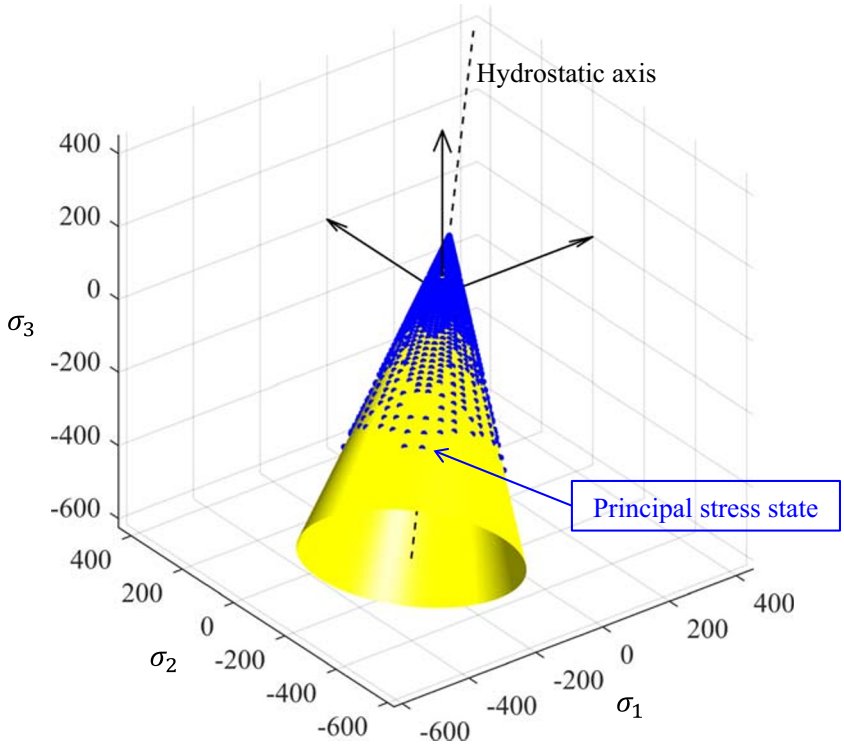

Fig. 3 Principal stress state representation. The yellow cone portrays the analytical Drucker–Prager strength surface, and the blue dots are the principal stress states of the surrogate nonlinear model. Notice that all the blue dots are located on the surface of the yellow cone, which verifies the model put forward by (1)

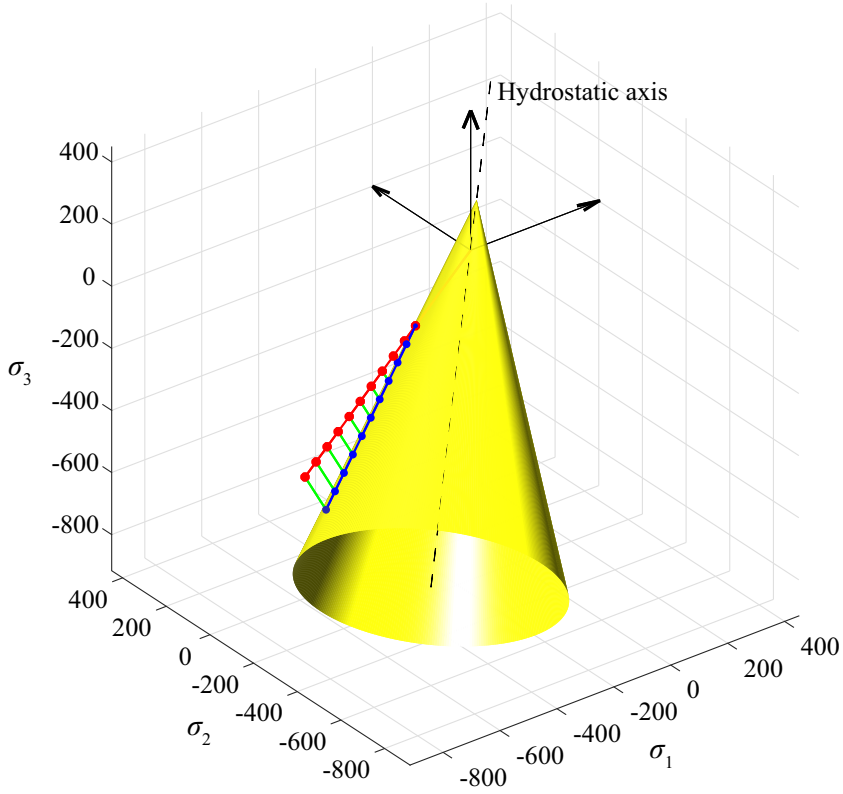

Fig. 4 Projection of the trial inadmissible elastic stress on the Drucker–Prager strength surface. The red line is the trajectory of the linear elastic trial stress state, and the blue line is the projected plastic stress state on the strength surface. The green lines connecting the red and blues dots are parallel and equally spaced. Those parallel lines indicate that the increment of the principal stresses on the strength surface is constant with respect to the increment of the principal strain

(24), $\boldsymbol{\varepsilon}'$, the interpolation of $\boldsymbol{\varepsilon}^L$ and the strain tensor $\boldsymbol{\varepsilon}$, is defined as follows:

$$\boldsymbol{\varepsilon}' = (1-t)\,\boldsymbol{\varepsilon}^L + t\,\boldsymbol{\varepsilon} \tag{26}$$

Since the increment of the stress components on the Drucker–Prager strength surface is constant with respect to the increment of the strain components (see Appendix C), we have:

$$\boldsymbol{\sigma}' = (1-t)\,\boldsymbol{\sigma}^L + t\,\boldsymbol{\sigma} \tag{27}$$

where $\boldsymbol{\sigma}'$ is the interpolation of $\boldsymbol{\sigma}^L$ and the stress tensor $\boldsymbol{\sigma}$. Substituting (27) into (24), then we obtain the explicit expression of the strain energy density as:

$$\varphi = \frac{1}{2}\left(\boldsymbol{\sigma}^L : \boldsymbol{\varepsilon} + \boldsymbol{\sigma} : \boldsymbol{\varepsilon} - \boldsymbol{\sigma} : \boldsymbol{\varepsilon}^L\right) \tag{28}$$

We know that both $\boldsymbol{\sigma}^L$ and $\boldsymbol{\varepsilon}^L$ in (28) can be expressed using the scalar t^L defined in (15) as:

$$\boldsymbol{\sigma}^L = t^L\boldsymbol{\sigma}^{tr}, \quad \boldsymbol{\varepsilon}^L = t^L\boldsymbol{\varepsilon} \tag{29}$$

Substituting (29) into (28), we rewrite the strain energy density φ in a more compact format as:

$$\boxed{\varphi = \frac{1}{2}\left[t^L(\boldsymbol{\sigma}^{\mathrm{tr}} - \boldsymbol{\sigma}) + \boldsymbol{\sigma}\right] : \boldsymbol{\varepsilon}'} \tag{30}$$

Region #3: apex zone if $f(\boldsymbol{\sigma}^{\mathrm{tr}}) > 0$ and $\phi_2 < 0$,

$$\varphi = \frac{1}{2}\boldsymbol{\sigma}^L : \boldsymbol{\varepsilon}^L + \int_{\boldsymbol{\varepsilon}^L}^{\boldsymbol{\varepsilon}^N} \boldsymbol{\sigma}' : d\boldsymbol{\varepsilon}' + \boldsymbol{\sigma}^N : \left(\boldsymbol{\varepsilon} - \boldsymbol{\varepsilon}^N\right) \tag{31}$$

where $\boldsymbol{\sigma}^N$ and $\boldsymbol{\varepsilon}^N$ are, respectively, the nonlinear elastic limit of the stress and strain tensor reached in the direction of strain $\boldsymbol{\varepsilon}$. $\boldsymbol{\sigma}'$ and $\boldsymbol{\varepsilon}'$ in (31) are defined as:

$$\boldsymbol{\varepsilon}' = t\boldsymbol{\varepsilon}, \quad \boldsymbol{\sigma}' = \frac{\boldsymbol{\sigma}^N - \boldsymbol{\sigma}^L}{t^N - t^L}\left(t - t^L\right) + \boldsymbol{\sigma}^L \tag{32}$$

By substituting (32) into (31) and recalling the two scaling factors t^L and t^N in (15), we obtain:

$$\varphi = \frac{1}{2}\boldsymbol{\sigma}^L : \boldsymbol{\varepsilon}^L + \int_{t^L}^{t^N}\left[\frac{\boldsymbol{\sigma}^N - \boldsymbol{\sigma}^L}{t^N - t^L}\left(t - t^L\right) + \boldsymbol{\sigma}^L\right] : \boldsymbol{\varepsilon}\,dt + \boldsymbol{\sigma}^N : \left(\boldsymbol{\varepsilon} - \boldsymbol{\varepsilon}^N\right) \tag{33}$$

The integral in (33) can be solved analytically. Then, we obtain the explicit expression of the strain energy density as:

$$\varphi = \frac{1}{2}\boldsymbol{\sigma}^L : \boldsymbol{\varepsilon}^L + \frac{1}{2}\left(t^N - t^L\right)\left(\boldsymbol{\sigma}^N + \boldsymbol{\sigma}^L\right) : \boldsymbol{\varepsilon} + \boldsymbol{\sigma}^N : \left(\boldsymbol{\varepsilon} - \boldsymbol{\varepsilon}^N\right) \tag{34}$$

Recall that we know $\boldsymbol{\sigma}^L = t^L\boldsymbol{\sigma}^{\mathrm{tr}}$, $\boldsymbol{\varepsilon}^L = t^L\boldsymbol{\varepsilon}$, and $\boldsymbol{\varepsilon}^N = t^N\boldsymbol{\varepsilon}$, then the strain energy density in (34) can be rewritten compactly as:

$$\boxed{\varphi = \frac{1}{2}\left[\left(2 - t^L - t^N\right)\boldsymbol{\sigma}^N + t^L t^N \boldsymbol{\sigma}^{\mathrm{tr}}\right] : \boldsymbol{\varepsilon}} \tag{35}$$

In summary, we have derived the analytical strain energy density functions, i.e., (23), (30), and (35), for the three possible stress states corresponding to three regions (i.e., linear elastic loading, nonlinear elastic loading, and apex zone). Those compact and explicit strain energy density functions contribute to a better understating of the nonlinear elastic constitutive model. In addition, the functions are associated with the objective (strain energy) of the optimization formulation in Section 3.

2.2 Material parameters transformation

From the aforementioned derivation, the material parameters υ^p and σ_y are required to define the nonlinear elastic constitutive model. However, from a practical point of view, these material parameters may not be convenient as some materials may be characterized by a given cohesion c and friction angle ψ, while some other materials may be defined by a given compressive strength σ_c and tensile strength σ_t. Therefore, transforming the given material parameters into the required parametric space is necessary.

2.2.1 Material model in terms of cohesion c and friction angle ψ

We derive the expression of υ^p and σ_y, respectively, in terms of c and ψ. The Drucker–Prager strength function can be defined in an alternative format such as:

$$F(\boldsymbol{\sigma}) = \frac{\eta}{3}J_1(\boldsymbol{\sigma}) + \sqrt{J_2(\boldsymbol{s})} - \zeta c \tag{36}$$

where c is the cohesion, and the parameters η and ζ are defined based on the required approximation to the Mohr–Coulomb criterion. We adopt the approximation which forces both Drucker–Prager and Mohr–Coulomb criteria to predict identical collapse load under plane strain conditions (Souza Neto et al. 2008). In this case, the parameters η and ζ are obtained as:

$$\eta = \frac{3\tan\psi}{\sqrt{9 + 12\tan^2\psi}}, \qquad \zeta = \frac{3}{\sqrt{9 + 12\tan^2\psi}} \tag{37}$$

By comparing (6) and (36), we have:

$$\beta = \frac{\eta}{3}, \quad k_s = \zeta c \tag{38}$$

According to (38), (37), and (8), we can express υ^p and σ_y, respectively, in terms of c and ψ:

$$\begin{aligned} \upsilon^p &= \frac{1}{2}\frac{\sqrt{3}\sqrt{9 + 12\tan^2\psi} - 6\tan\psi}{\sqrt{3}\sqrt{9 + 12\tan^2\psi} + 3\tan\psi} \\ \sigma_y &= \frac{9c}{\sqrt{3}\sqrt{9 + 12\tan^2\psi} + 3\tan\psi} \end{aligned} \tag{39}$$

2.2.2 Material model in terms of σ_c and σ_t

We express υ^p and σ_y, respectively, in terms of σ_c and σ_t. Inspired by Luo and Kang (2012), we substitute two specific principal stress states ($\sigma_1 = \sigma_2 = 0$ & $\sigma_3 = -\sigma_c$) and ($\sigma_1 = \sigma_t$ & $\sigma_2 = \sigma_3 = 0$) into the strength condition, i.e., (6), as follows:

$$-\beta\sigma_c + \frac{\sigma_c}{\sqrt{3}} - k_s = 0, \qquad \beta\sigma_t + \frac{\sigma_t}{\sqrt{3}} - k_s = 0 \tag{40}$$

By solving (40), we obtain that:

$$\beta = \frac{\sigma_c - \sigma_t}{\sqrt{3}(\sigma_c + \sigma_t)}, \qquad k_s = \frac{2\sigma_c\sigma_t}{\sqrt{3}(\sigma_c + \sigma_t)} \tag{41}$$

According to (41) and (8), we can express υ^p and σ_y, respectively, in terms of σ_c and σ_t as follows:

$$\upsilon^p = \frac{3\sigma_t - \sigma_c}{4\sigma_c}, \qquad \sigma_y = \sigma_t \tag{42}$$

3 Optimization formulation and sensitivity analysis

We present our topology optimization framework based on a nested formulation for maximizing the structural strain energy with prescribed energy input. Moreover, we point out the simplicity, efficiency, and accuracy of sensitivity evaluation using our formulation.

3.1 Nested formulation: maximizing structural strain energy

We consider a nested formulation for the optimization problem by maximizing the structural strain energy with prescribed energy in the nonlinear state equations:

$$\max_{\boldsymbol{\rho}} \; J_U(\boldsymbol{\rho}) \coloneqq U(\boldsymbol{\rho}, \boldsymbol{u}(\boldsymbol{\rho}))$$
$$\text{s.t.} \begin{cases} \sum_{e=1}^{n} \rho_e v_e \leq V_{max} \\ 0 < \rho_{min} \leq \rho_e \leq 1 \end{cases} \tag{43}$$
$$\text{with} \begin{cases} \boldsymbol{T}(\boldsymbol{\rho}, \boldsymbol{u}(\boldsymbol{\rho})) = \chi(\boldsymbol{\rho}, \boldsymbol{u}(\boldsymbol{\rho}))\boldsymbol{f}_0 \\ \boldsymbol{f}_0^{\mathrm{T}} \boldsymbol{u}(\boldsymbol{\rho}) = 2C_0 \end{cases}$$

In the optimization problem, the objective function $U(\boldsymbol{\rho}, \boldsymbol{u}(\boldsymbol{\rho}))$ is the structural strain energy, given by the integration of the strain energy density function φ (see Section 2.1) over the domain. The design variable $\boldsymbol{\rho}$ is a vector of element material densities. The parameter n represents the number of elements used to discretize the design domain, v_e is the volume of element e, $V_{\max}$ is the maximum material volume (constraint), and $\rho_{\min}$ denotes the lower bound of the design variable (e.g., 10^{-4}), which is introduced to prevent numerical singularity in the design domain (Bendsøe and Sigmund 2003). In the state problem, $\boldsymbol{T}(\boldsymbol{\rho}, \boldsymbol{u}(\boldsymbol{\rho}))$ is the internal force vector, $\chi(\boldsymbol{\rho}, \boldsymbol{u}(\boldsymbol{\rho}))$ is the reaction load factor, $\boldsymbol{f}_0$ is the vector of given external forces, and C_0 is the prescribed energy in the structural system. For structures subjected to prescribed energy and given fixed supports, maximizing the structural strain energy is equivalent to maximizing the load capacity, i.e., reaction load factor (Zhao et al. 2019), which is verified through the numerical examples later in this paper (see Sections 4.2 and 4.3). In the case of linear elasticity, we could achieve the same results as the maximum structural stiffness problem (Niu et al. 2011).

We adopt a unified optimization scheme both for the solution of the state equation and for the topology optimization phase. Finding a solution of the state equations in (43) is equivalent to solving the following equality constrained minimization problem (Boyd and Vandenberghe 2004):

$$\begin{cases} \min_{\boldsymbol{u}} U(\boldsymbol{\rho}, \boldsymbol{u}(\boldsymbol{\rho})) \\ s.t. \;\; \boldsymbol{f}_0^T \boldsymbol{u} = 2C_0 \end{cases} \tag{44}$$

which can be solved, for example, using Newton's method with an inexact line search strategy (see Appendix D).

We introduce a set $\mathcal{A}$ to replace the constraint in (44), which is given by:

$$\mathcal{A} = \left\{ \boldsymbol{u} \mid \boldsymbol{f}_0^T \boldsymbol{u} = 2C_0 \right\} \tag{45}$$

Then, the state problem (44) can be rearranged using unconstrained optimization:

$$\min_{\boldsymbol{u} \in \mathcal{A}} U(\boldsymbol{\rho}, \boldsymbol{u}(\boldsymbol{\rho})) \tag{46}$$

Now, we can reformulate the objective function $J_U(\boldsymbol{\rho})$ in (43) as the min-max formulation described in (Klarbring and Strömberg 2012):

$$\boxed{\max_{\boldsymbol{\rho}} \; J_U(\boldsymbol{\rho}) = \max_{\boldsymbol{\rho}} \; \min_{\boldsymbol{u} \in \mathcal{A}} U(\boldsymbol{\rho}, \boldsymbol{u}(\boldsymbol{\rho}))} \tag{47}$$

where the inner optimization statement (min) refers to the state equation solution phase and the outer one (max) refers to the topology optimization phase. The sensitivity of this objective in (47) can be simply calculated as:

$$\boxed{\frac{dJ_U(\boldsymbol{\rho})}{d\rho_e} = \frac{\partial U(\boldsymbol{\rho}, \boldsymbol{u}(\boldsymbol{\rho}))}{\partial \rho_e}} \tag{48}$$

which is quite elegant. Notice that there is no need for introducing an extra adjoint problem because the formulation of maximizing structural strain energy is self-adjoint. When compared with the standard approach (see, for example, Alberdi and Khandelwal 2017), the sensitivity analysis utilized here is simple, effective, and efficient.

The structural strain energy function $U(\boldsymbol{\rho}, \boldsymbol{u}(\boldsymbol{\rho}))$ is defined using the following expression:

$$U(\boldsymbol{\rho}, \boldsymbol{u}(\boldsymbol{\rho})) = \sum_{e=1}^{n} \int_{V_e} \varphi_e(\boldsymbol{\rho}, \boldsymbol{u}(\boldsymbol{\rho})) dV \tag{49}$$

where $\varphi_e(\boldsymbol{\rho}, \boldsymbol{u}(\boldsymbol{\rho}))$ is the strain energy density function of element e. Substituting (49) into (48), the sensitivity of the objective is obtained as follows:

$$\frac{dJ_U(\boldsymbol{\rho})}{d\rho_e} = \sum_{e=1}^{n} \int_{V_e} \frac{\partial \varphi_e(\boldsymbol{\rho}, \boldsymbol{u}(\boldsymbol{\rho}))}{\partial \rho_e} dV \tag{50}$$

Recall that from the analytical strain energy density functions in (23), (30), and (35), we need to calculate the corresponding derivatives considering three different regions. First, in the region of linear elastic loading, the derivative of the strain energy density function in (23) is:

$$\frac{\partial \varphi}{\partial \rho_e} = \frac{1}{2} \frac{\partial \boldsymbol{\sigma}^{\mathrm{tr}}}{\partial \rho_e} : \boldsymbol{\varepsilon} \tag{51}$$

Second, considering nonlinear elastic loading, the derivative of (30) is:

$$\frac{\partial \varphi}{\partial \rho_e} = \frac{1}{2} \left[\frac{\partial t^L}{\partial \rho_e} (\boldsymbol{\sigma}^{\mathrm{tr}} - \boldsymbol{\sigma}) + t^L \left(\frac{\partial \boldsymbol{\sigma}^{\mathrm{tr}}}{\partial \rho_e} - \frac{\partial \boldsymbol{\sigma}}{\partial \rho_e} \right) + \frac{\partial \boldsymbol{\sigma}}{\partial \rho_e} \right] : \boldsymbol{\varepsilon} \tag{52}$$

Third, we obtain the derivative of the strain energy density function in (35) as:

$$\frac{\partial \varphi}{\partial \rho_e} = \frac{1}{2} \left[\left(-\frac{\partial t^L}{\partial \rho_e} - \frac{\partial t^N}{\partial \rho_e} \right) \boldsymbol{\sigma}^N + \left(\frac{\partial t^L}{\partial \rho_e} t^N + t^L \frac{\partial t^N}{\partial \rho_e} \right) \boldsymbol{\sigma}^{\mathrm{tr}} + t^L t^N \frac{\partial \boldsymbol{\sigma}^{\mathrm{tr}}}{\partial \rho_e} \right] : \boldsymbol{\varepsilon} \tag{53}$$

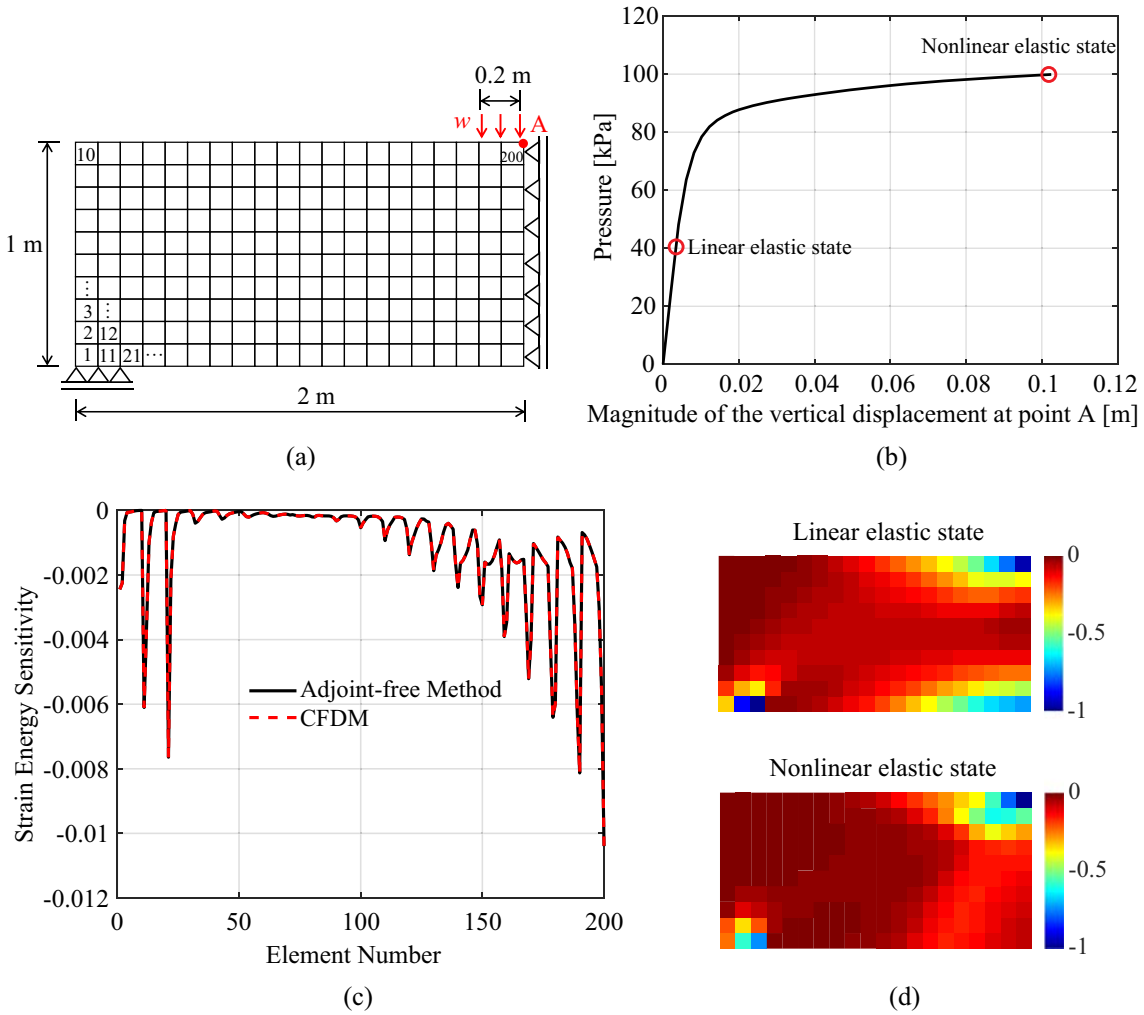

Fig. 5 Verification of the sensitivity analysis. **a** Half-beam domain with element numbers, boundary, and loading conditions. **b** Structural behavior of the beam: applied pressure versus magnitude of the vertical displacement at point A in the domain. The two representative states, i.e., a linear elastic state and a nonlinear elastic state, are indicated in the plot. **c** Strain energy sensitivities at the nonlinear elastic state: adjoint-free solution (i.e., (50)) matches the one obtained using CFDM. **d** Contour plots of the normalized sensitivity vector obtained from the adjoint-free method when the structure is in either the linear elastic state or the nonlinear elastic state

3.2 Verification of sensitivity analysis

In this section, we verify the sensitivity analysis by comparing the solutions obtained from (50) with the results calculated using the central finite difference method (CFDM). Considering CFDM, we obtain the sensitivity of the strain energy function U with respect to a design variable ρ_e:

$$\frac{dU(\boldsymbol{\rho})}{d\rho_e} \approx \frac{U(\boldsymbol{\rho}+\Delta\boldsymbol{\rho})-U(\boldsymbol{\rho}-\Delta\boldsymbol{\rho})}{2\Delta\rho_e} \tag{54}$$

where $\Delta\boldsymbol{\rho}$ is a vector containing all zero components except at the element related to ρ_e. The only non-zero component $\Delta\rho_e$ is taken as 10^{-6} in this verification study. We consider a half-beam domain, which is discretized into a 20 by 10 mesh. The element numbers of the mesh are shown in Fig. 5(a). We use a uniform value of 1 for the densities in all of the elements, and no density filter is used. A reference distributed load with the magnitude of $w = 15$ kN/m is applied on a 0.2 m portion of the bottom of the beam. The material properties used in the verification are listed in Table 1.

Table 1 Material properties used in the sensitivity verification example

Property	Symbol	Magnitude
Young's modulus	E	6.5×10^4 kPa
Poisson's ratio	υ	0.3
Friction angle	ψ	20°
Cohesion stress	c	50 kPa

Table 2 Brief description of the numerical examples

Example	Description	Remarks
1	Corner-supported square (Swan and Kosaka 1997)	• Optimized topology agrees with the benchmark problem considering the Drucker–Prager criterion • Proper convergence in both optimization and FEM • Advantage of inexact line search in solving nonlinear state equations • The particular case of identical material strength in compression and tension is investigated, which simplifies to the von Mises criterion
2	Clamped beam	• Nonlinear solutions are obtained with different prescribed energy C_0 • Convergence plot for max$U$ formulation exhibits smooth behavior
3	Structural performance of the optimized clamped beams	• Verification of topologically optimized structures using commercial FEA software • Comparison of structural performance using the standard Drucker–Prager plasticity and those considering the nonlinear elastic model • The nonlinear elastic solution is analogous to the plasticity solution
4	Beams with pin/roller supports	• Nonlinear solutions are investigated with two types of support conditions

We define the value of the prescribed energy as $C_0 = 0.15$ kJ. The structural response in Fig. 5(b) indicates that the beam undergoes nonlinear deformation. In the nonlinear elastic state highlighted in Fig. 5(b), we calculate the strain energy sensitivities using both the adjoint-free method and CFDM for each element. Figure 5(c) compares the results obtained from the two approaches. To quantify the comparison, we set up a measurement using the relative error defined as follows:

$$\text{Relative error} = \frac{\left| \left(\frac{dU}{d\rho_e}\right)_{\text{adjoint-free}} - \left(\frac{dU}{d\rho_e}\right)_{\text{CFDM}} \right|}{1 + \left| \left(\frac{dU}{d\rho_e}\right)_{\text{CFDM}} \right|} \tag{55}$$

It is shown that adjoint-free sensitivities closely match those obtained using CFDM with relative errors in the order of 10^{-9}. In Fig. 5(d), we compare the contour plots of the normalized sensitivities for two different states, i.e., linear elastic state and the nonlinear elastic state, respectively. The comparison indicates that the strain energy sensitivities vary as the structure behavior switches from the linear state to the nonlinear state. Furthermore, different sensitivities will lead to various optimal solutions (see examples in Section 4).

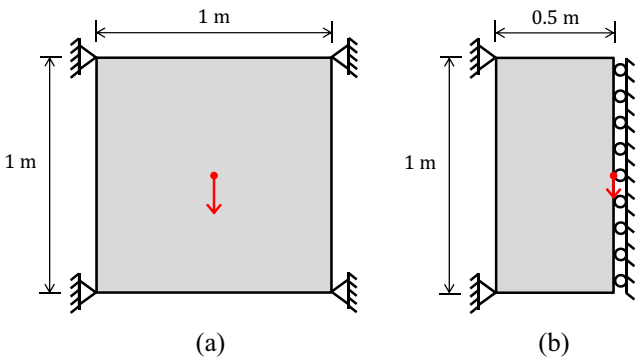

Fig. 6 **a** Idealized geometry, loading, and support conditions of the corner-supported square problem. **b** A half of the square is used as a design domain with symmetry boundary conditions

4 Numerical examples

Four numerical examples demonstrate the key features of the present material nonlinear topology optimization approach considering the Drucker–Prager strength criterion. A summary of the examples is provided in Table 2.

4.1 Corner-supported square

We first present a corner-supported square example to illustrate the behavior of the proposed nonlinear topology optimization framework considering the Drucker–Prager criterion. Figure 6(a) shows the geometry and dimensions of the square domain. A reference point load with a magnitude of 1 MN is applied to the center of the square. Due to symmetry, only half of the square shown in Fig. 6(b) is considered as a design domain with the symmetry boundary conditions. The design domain is discretized with 6272 quadrilateral elements under plane strain conditions. The material properties used in the numerical simulation

Table 3 Material properties used in the corner-supported square problem

Property	Symbol	Magnitude
Young's modulus	E	1×10^5 MPa
Poisson's ratio	υ	0.3
Tensile strength	σ_t	10 MPa or 40 MPa
Compressive strength	σ_c	40 MPa

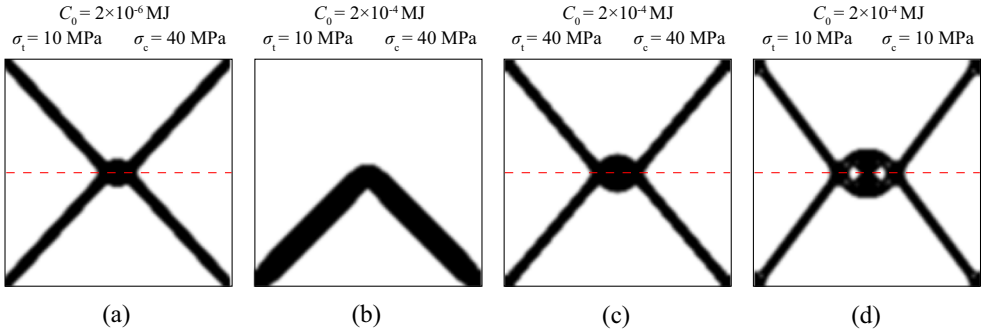

Fig. 7 Optimized solutions of the corner-supported square problem considering (**a**) $C_0 = 2 \times 10^{-6}$ MJ, $\sigma_t = 10$ MPa, $\sigma_c = 40$ MPa; (**b**) $C_0 = 2 \times 10^{-4}$ MJ, $\sigma_t = 10$ MPa, $\sigma_c = 40$ MPa; (**c**) $C_0 = 2 \times 10^{-4}$ MJ, $\sigma_t = \sigma_c = 40$ MPa; (**d**) $C_0 = 2 \times 10^{-4}$ MJ, $\sigma_t = \sigma_c = 10$ MPa. The horizontal-dashed lines represent line of symmetry

are listed in Table 3. In this problem, we utilize the solid isotropic material with penalization (SIMP) model (Bendsøe 1989; Rozvany et al. 1992; Bendsøe and Sigmund 1999; Rozvany 2009) with constant penalization parameter using $p = 3$. The other optimization parameters are given as follows: volume fraction VolFrac = 15% , and a linear density filter (Borrvall and Petersson 2001; Bourdin 2001) radius $R = 0.018$ m. As usual, the SIMP design optimization problem is solved by the optimality criteria (OC) approach.

Figure 7 presents the optimized topologies for the corner-supported square problem considering different prescribed energy C_0 and different material strength (i.e., σ_t & σ_c). Considering a small value of the prescribed energy $C_0 = 8 \times 10^{-6}$ MJ, the optimized topology is shown in Fig. 7(a). As expected, this topology is identical to the result obtained considering a linear elastic material constitutive model. When a lager prescribed energy is utilized (i.e., $C_0 = 2 \times 10^{-4}$ MJ), Fig. 7(b), (c) and (d) show the nonlinear solutions considering the material strength $\sigma_c = 4\sigma_t = 40$ MPa, $\sigma_c = \sigma_t = 40$ MPa, and $\sigma_c = \sigma_t = 10$ MPa, respectively. When the compressive strength and tensile strength are the same, the proposed nonlinear elastic model obeys the von Mises criterion. In addition, the final topologies considering linear elastic and von Mises cases (i.e., Fig. 7(a), (c), and (d)) present symmetry with a horizontal line, while the final topology (i.e., Fig. 7(b)) accounting for different material strength in compression and tension does not have the horizontal line of symmetry. The optimized topology of Fig. 7(b) agrees with the results by Swan and Kosaka (1997) considering the standard plasticity formulation. Furthermore, Table 4 includes the objective (i.e., strain energy U) and the corresponding load factor χ obtained in the solution. Considering the same prescribed energy, i.e., $C_0 = 2 \times 10^{-4}$ MJ, we observe that the load factors are quite different for the three cases because of the different material strengths.

The proposed nonlinear topology optimization framework considering the Drucker–Prager criterion has good convergence behavior in both optimization and FEM schemes. For example, Fig. 8 illustrates the convergence of optimization using the prescribed energy $C_0 = 2 \times 10^{-4}$ MJ. The intermediate topologies at iteration #6, #70, and #608 are shown in Fig. 8. It is clear that the convergence curve is smooth. Moreover, the nonlinear FEM iterations at optimization iteration no. 6 are shown in Table 5. The case with the line search approach converges within 13 FEM iterations, while the case without

Table 4 Results of the square problem considering different prescribed energy C_0

C_0 (MJ)	σ_t (MPa)	σ_c (MPa)	U (MJ)	χ
2×10^{-6}	10	40	4.65×10^{-8}	2.33×10^{-2}
2×10^{-4}	10	40	4.06×10^{-4}	2.01
2×10^{-4}	40	40	3.40×10^{-4}	1.39
2×10^{-4}	10	10	1.72×10^{-4}	5.82×10^{-1}

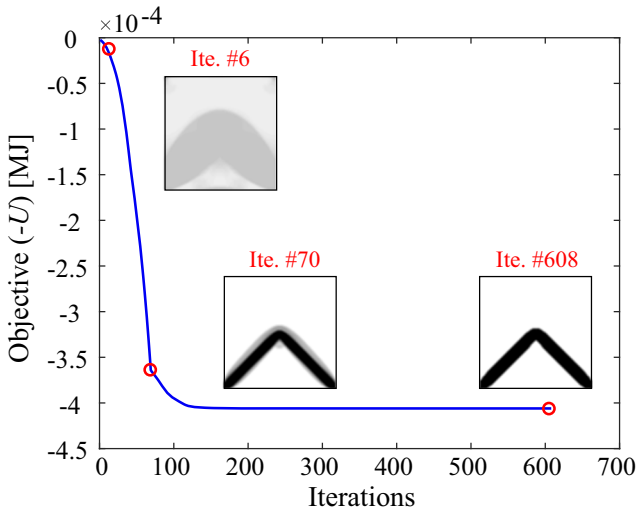

Fig. 8 Convergence of optimization considering max$U$ formulation with the prescribed energy $C_0 = 2 \times 10^{-4}$ MJ, and material strength $\sigma_c = 4\sigma_t = 40$ MPa

Table 5 Convergence of FE solutions for the square problem at optimization iteration no. 6 considering $C_0 = 2 \times 10^{-4}$ MJ and $\sigma_c = 4\sigma_t = 40$ MPa. Note the influence of the inexact line search approach. If the line search is not used, then the Newton's method does not converge

Newton's method ***with line search***		
FEM iter.	Step size	$\frac{\|\Delta \boldsymbol{u}\|}{1+\|\boldsymbol{u}\|}$
1	4.37×10^{-1}	1.65×10^{-3}
2	4.09×10^{-1}	8.66×10^{-4}
3	4.31×10^{-1}	5.98×10^{-4}
4	1.00	9.25×10^{-4}
5	1.00	9.80×10^{-5}
6	1.00	3.35×10^{-5}
7	1.00	1.23×10^{-5}
8	1.00	1.36×10^{-5}
9	1.02×10^{-1}	1.73×10^{-6}
10	3.55×10^{-1}	4.73×10^{-6}
11	1.00	2.80×10^{-6}
12	3.92×10^{-2}	1.61×10^{-7}
13	9.31×10^{-10}	3.75×10^{-15}

the line search fails to converge. Thus, this example highlights the relevance of the line search method. As a comparison, a path-dependent model often tends to have difficulty in convergence. Utilizing the present nonlinear elastic constitutive model, we can solve both the optimization problem and the nonlinear state problem and achieve converged results.

4.2 Clamped beam

The clamped beam example is presented next to further illustrate the behavior of the proposed material nonlinear topology optimization framework. Figure 9 shows the geometry and dimensions of the beam, which is fixed at both left and right ends. A distributed load with the magnitude of $w = 80$ MN/m is applied on a 0.25-m portion of the bottom of the beam. Only half of the clamped beam is considered for the design domain as symmetry boundary conditions are considered. We adopt a mesh discretization with 6272 quadrilateral elements under plane strain conditions. The material properties of the beam are listed in Table 6. The optimization parameters are given as follows: a volume fraction VolFrac = 25%, a linear filter radius $R = 0.01429$ m, and the SIMP model with a constant penalization parameter $p = 3$.

Table 6 Material properties used in the clamped beam problem

Property	Symbol	Magnitude
Young's modulus	E	1.8×10^5 MPa
Poisson's ratio	υ	0.3
Tensile strength	σ_t	144 MPa
Compressive strength	σ_c	1440 MPa

Figure 10 shows the optimized topologies with different prescribed energy C_0. Figure 10(a) presents the optimized result considering a small prescribed energy $C_0 = 8 \times 10^{-4}$ MJ. As expected, this topology is identical to the linear elastic result obtained using the educational code PolyTop (Talischi et al. 2012). Figure 10(b) and (c) show the nonlinear solutions considering $C_0 = 1.1 \times 10^{-2}$ MJ and $C_0 = 1.3 \times 10^{-2}$ MJ, respectively. Moreover, as we further increase the prescribed energy C_0, the topology of the optimized solution remains the same as the one in Fig. 10(c), and thus, we can estimate a limit value of C_0 for a given volume fraction (see details in the Appendix B). With different values of the prescribed energy, the material can be in various states, which leads to different sensitivities. Thus, the corresponding optimized topologies in Fig. 10 are quite different. Table 7 shows that the topology in Fig. 10(c) has larger reaction load factor than the topologies in Fig. 10(b) and (c). This observation verifies that the physical meaning of the objective function is to maximize the structural loading capacity.

We further investigate the stress state of the nonlinear solution obtained with $C_0 = 1.3 \times 10^{-2}$ MJ, as shown in

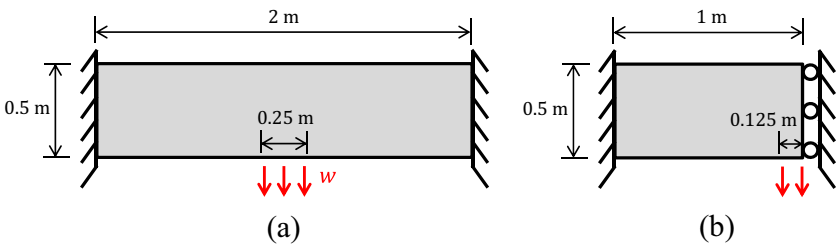

Fig. 9 **a** Geometry, loading, and support conditions of the clamped beam problem. **b** Half of the beam is used as a design domain with symmetry boundary conditions

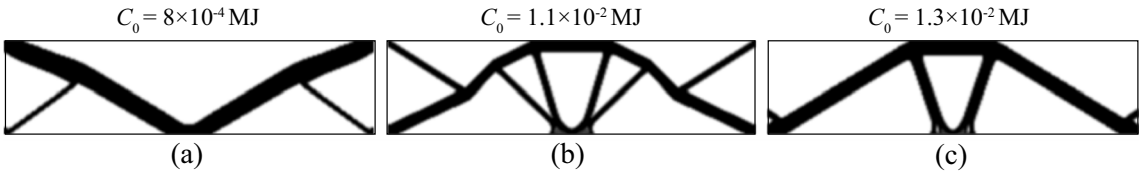

Fig. 10 Optimized topologies of the clamped problem considering (**a**) $C_0 = 8 \times 10^{-4}$ MJ, (**b**) $C_0 = 1.1 \times 10^{-2}$ MJ, and (**c**) $C_0 = 1.3 \times 10^{-2}$ MJ

Table 7 Results of clamped beam problem considering different prescribed energy C_0

C_0 (MJ)	U (MJ)	χ
8×10^{-4}	4.50×10^{-5}	5.68×10^{-2}
1.1×10^{-2}	7.12×10^{-3}	6.36×10^{-1}
1.3×10^{-2}	9.49×10^{-3}	7.21×10^{-1}

Fig. 11(a). The distribution of the (absolute) maximum principal stress in Fig. 11(b) shows the structural members either in compression or tension. By plotting the contour of the Drucker–Prager strength function (i.e., (6)) in Fig. 11(c), we observe that the stress state of tension members reaches the strength limit while the stress state of compression members remains in the linear elastic region. This observation is supported by the nature of the selected Drucker–Prager material, which has high compressive strength but low tensile strength.

Figure 12 illustrates the convergence history of the clamped beam problem with the prescribed energy $C_0 = 1.3 \times 10^{-2}$ MJ. The intermediate topologies at iteration #10, #50, and #300 are shown in the figure. This study indicates that the present nonlinear elastic optimization framework has proper convergence behavior.

4.3 Structural performance of the three optimized clamped beams

We verify the structural performance of the three topologically optimized clamped beam structures (which are obtained in the previous Section 4.2) in ABAQUS® composed of two different material constitutive models, namely the built-in Drucker–Prager plasticity model and the present surrogate nonlinear elastic model (the UMAT file is provided in Appendix E).

At first, three optimized topologies are digitized and converted to CAD models in ABAQUS®. To define the solid boundaries of topologies, we consider densities (i.e., design variables) $\rho > 0.5$ (cutoff) to be solid (Zegard and Paulino 2016). This approach allows us to represent the boundaries of the topologies by contour lines while satisfying the volume constraint. The con-

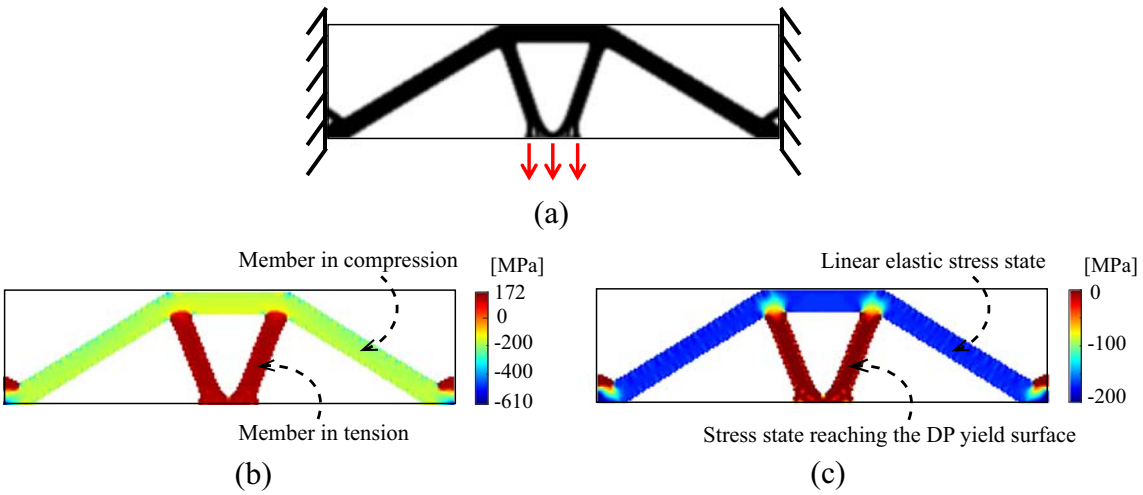

Fig. 11 (**a**) Nonlinear solution obtained considering $C_0 = 1.3 \times 10^{-2}$ MJ. (**b**) The distribution of the (absolute) maximum principal stress. (**c**) The contour plot of the Drucker–Prager (DP) strength function in (6)

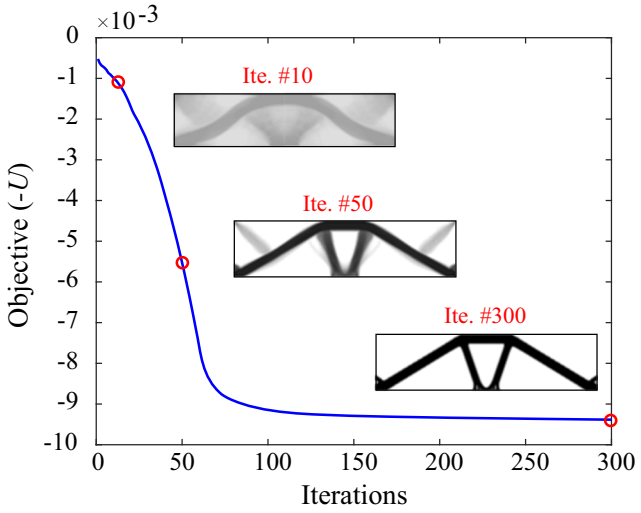

Fig. 12 Convergence of optimization for the clamped beam using max$U$ formulation under the prescribed energy $C_0 = 1.3 \times 10^{-2}$ MJ

tour lines can be imported into AutoCAD as polylines and then exported as a standard ACIS file, which later can be imported into ABAQUS®. Figure 13 shows the CAD models in ABAQUS®, named as topologies I, II, and III with volumes 0.2462, 0.2466, and 0.2454, respectively. Notice that the volume fraction is 25% (i.e., the upper bound volume is $2 \times 0.5 \times 25\% = 0.25$) in this optimization of the clamped beam problem. In ABAQUS®, topologies I, II, and III are discretized by 6145, 6106, and 6171 linear triangular elements of type CPE3, respectively, under plane strain conditions.

Secondly, we define the material properties for the plasticity model and nonlinear elastic model, respectively. In ABAQUS®, we choose the built-in Drucker–Prager plasticity model with the hardening behavior type defined by the linear shear criterion. We assume associated flow (i.e., the friction angle is identical to the dilation angle), and the flow stress

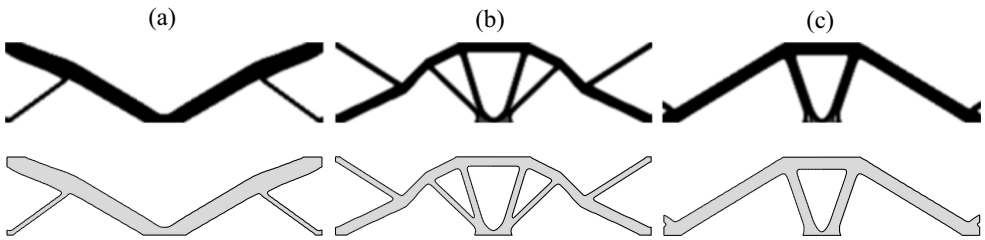

Fig. 13 The optimized clamped beam structure considering (**a**) linear elastic material, (**b**) Drucker–Prager material with the prescribed energy $C_0 = 1.1 \times 10^{-2}$ MJ, and (**c**) Drucker–Prager material with $C_0 = 1.3 \times 10^{-2}$ MJ. The second row shows the digitized structures which are converted to CAD models in ABAQUS®. The corresponding topologies on the second row are named topologies I, II, and III, respectively

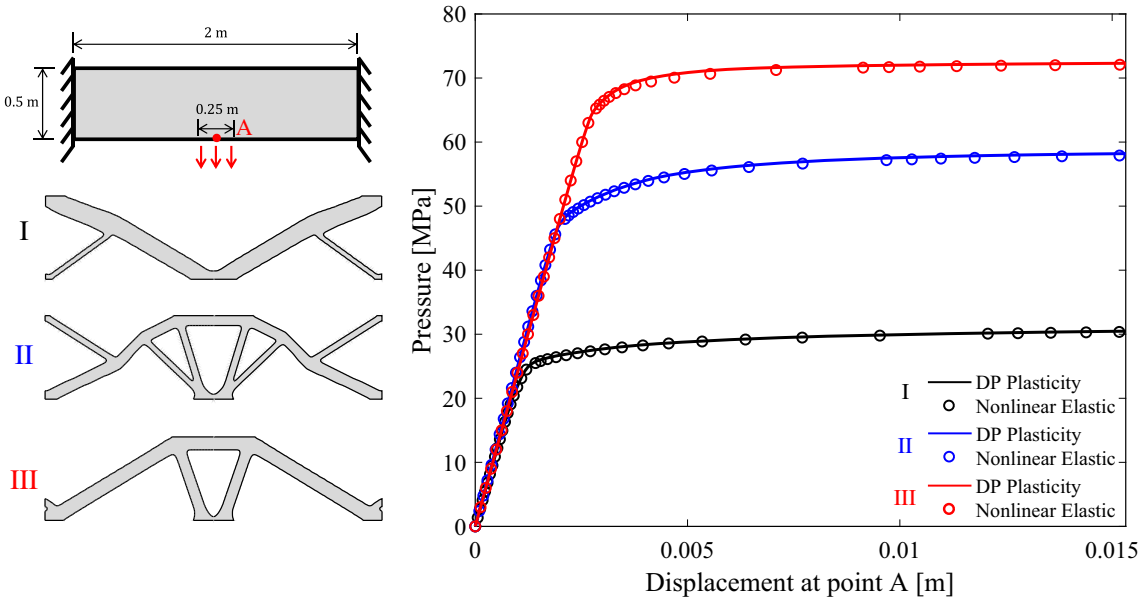

Fig. 14 Structural performance of the three optimized topologies I, II, and III. The solid lines and the small circles represent the structural behavior considering the Drucker–Prager plasticity and the surrogate nonlinear elastic model, respectively

Table 8 The limit pressure for topologies I, II, and III considering the Drucker–Prager plasticity model and the surrogate nonlinear elastic model

Topology	Limit pressure (MPa)	
	Drucker–Prager plasticity	Nonlinear elastic
I	30.464	30.362
II	58.200	57.900
III	72.298	72.075

Table 9 Material properties used in the beam problem with two types of support conditions

Property	Symbol	Magnitude
Young's modulus	E	1.8×10^5 MPa
Poisson's ratio	υ	0.3
Tensile strength	σ_t	144 MPa
Compressive strength	σ_c	1440 MPa

ratio is equal to 1. Given the material tensile strength and compressive strength (i.e., $\sigma_t = 144$ MPa, $\sigma_c = 1440$ MPa) which are the same as the ones defined in the second numerical example, we can calculate the input data for the Drucker–Prager plasticity model with the associated flow in ABAQUS®, i.e., friction angle $\psi = 67.83^{\circ}$, shear (cohesion) strength stress $c = 261.82$ MPa, and select "linear" as the shear criterion. On the other hand, based on (42), we obtain the input data for the nonlinear elastic model in the UMAT file as $\upsilon^p = -0.175$ and $\sigma_y = 144$ MPa. For both the plasticity and the nonlinear elastic models, we define $E = 1.8 \times 10^5$ MPa and $\upsilon = 0.3$.

Lastly, the general static algorithm is used for a solution under prescribed pressure load. The simulation is performed under small deformation, so the *Nlgeom* option in ABAQUS® is turned off. Increasing pressure is applied to these three topologies until the magnitude of the vertical displacement at point A (as shown in Fig. 14) reaches 0.015 m. The structural performance of the topologies is investigated, considering both the plasticity model and the nonlinear elastic model. For the plasticity model, we obtain the behavior of the structures shown as solid curves in Fig. 14. Each curve represents the applied pressure versus the vertical displacement at point A of the clamped beam. For the nonlinear elastic model, the behavior of the structures is represented by the small circles shown in Fig. 14. The limit pressures for topology I, II, and III, considering the two different material constitutive models, are listed in Table 8. We notice that the limit pressures obtained using the nonlinear elastic model are similar to those obtained using the plasticity model.

4.4 Beams with pin/roller supports

In this section, a beam with two types of support conditions (i.e., pin-pin and pin-roller) is investigated by the present nonlinear topology optimization framework considering the Drucker–Prager criterion. The geometry, dimensions, loading, and support conditions are shown in Fig. 15(a) and (b). The magnitude of applied distributed loads is $w = 55$ MN/m. The material properties used in the numerical simulation are listed in Table 9. By applying the symmetry boundary conditions, only half of the beam is considered as a design domain, which is discretized with 5000 quadrilateral elements under plane strain conditions. We use the following optimization parameters: volume fraction is VolFrac = 30%, linear density filter radius $R = 0.06$ m, and the SIMP model with constant penalization parameter, $p = 3$.

For the pin-pin support conditions, the optimized topologies are presented in Fig. 16. Figure 16(a) shows the result considering a small prescribed energy $C_0 = 5 \times 10^{-5}$ MJ. As expected, this topology is identical to the linear elastic result obtained using the educational code PolyTop (Talischi et al. 2012). When a larger prescribed energy $C_0 = 0.2$ MJ is applied, we obtain a nonlinear solution as shown in Fig. 16(b), which has a different topology than the linear solution. The

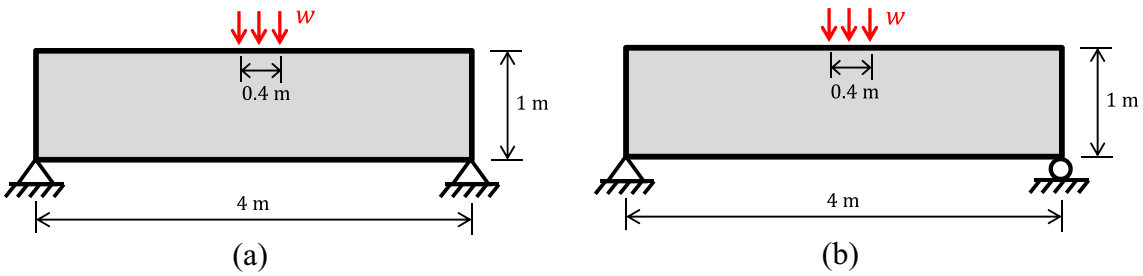

Fig. 15 Geometry, loading, and support conditions of the beam problem with (**a**) pin-pin supports and (**b**) pin-roller supports

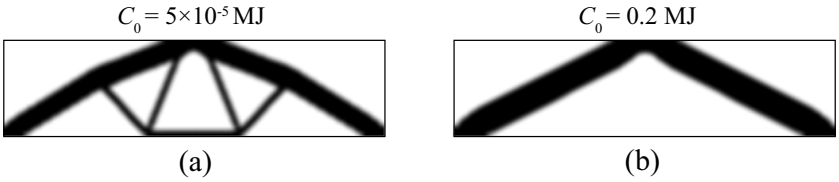

Fig. 16 Results of the beam problem with **pin-pin** support conditions. The optimized topologies considering (**a**) $C_0 = 5 \times 10^{-5}$ MJ and (**b**) $C_0 = 0.2$ MJ

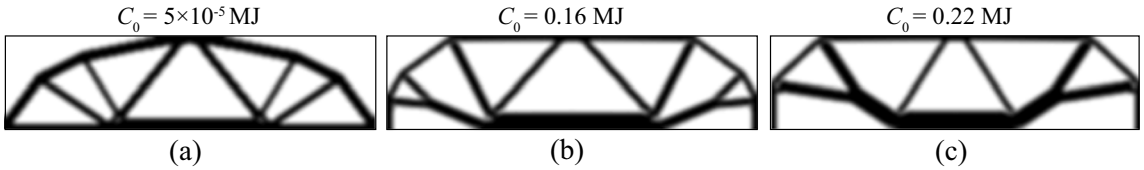

Fig. 17 Results of the beam with **pin-roller** support conditions. The optimized topologies considering (**a**) $C_0 = 5 \times 10^{-5}$ MJ, (**b**) $C_0 = 0.16$ MJ, and (**c**) $C_0 = 0.22$ MJ

objective (i.e., strain energy U) and related load factor χ of those solutions are listed in Table 10.

For the pin-roller support condition, Fig. 17 shows the optimized solutions considering different prescribed energy. The topology in Fig. 17(a) is the same as the one obtained using PolyTop (Talischi et al. 2012), considering a linear elastic material. Figure 17(b) and (c) illustrate the nonlinear solutions considering $C_0 = 0.16$ MJ and $C_0 = 0.22$ MJ, respectively. We observed that the topologies obtained using different prescribed energy are quite distinct. Table 10 includes a comparison of the objective (U) and related load factor (χ) for those solutions.

5 Concluding remarks

This paper addresses material nonlinear topology optimization problem considering the Drucker–Prager criterion using a surrogate nonlinear elastic model. With this nonlinear elastic model, the sensitivity analysis is quite effective and efficient in the sense that there is no extra adjoint equation (since the problem is self-adjoint). A nested optimization formulation by maximizing the structural strain energy (max$U$) is presented. We consider the topology optimization problem subjected to a certain prescribed energy—we prescribe a certain value of energy C_0 for all design cycles until an optimal design is reached. This prescribed energy approach leads to robust convergence in all the nonlinear problems investigated. The nonlinear state equations are solved using direct minimization of the structural strain energy employing Newton's method with an inexact line search strategy, which improves the convergence of the nonlinear FEM. Four numerical examples demonstrate the features of the approach. All the optimization problems accounting for the Drucker–Prager criterion have smooth convergence when considering the present nonlinear elastic formulation.

Table 10 Results of the beam problem with two types of support conditions

Support condition	Case 1			Case 2			Case 3		
	C_0 (MJ)	U (MJ)	χ	C_0 (MJ)	U (MJ)	χ	C_0 (MJ)	(MJ)	χ
Pin-pin	5×10^{-5}	1.3×10^{-7}	2.5×10^{-3}	0.2	2.13	10.64	–		
Pin-roller	5×10^{-5}	5.3×10^{-8}	1.1×10^{-3}	0.16	0.27	1.20	0.22	0.41	1.31

Acknowledgments This paper is dedicated to the memory of Robert Hooke (July 28, 1635 – March 3, 1703).

Funding Information GHP and TZ acknowledge the financial support from the US National Science Foundation under project #1663244 and the endowment provided by the Raymond Allen Jones Chair at the Georgia Institute of Technology. ASR Jr. and ENL appreciate the financial support from the Brazilian National Council for Research and Development (CNPq). The information in this paper is the sole opinion of the authors and does not necessarily reflect the views of the sponsoring agencies.

Compliance with ethical standards

Conflict of interest The authors declare that they have no conflict of interest.

Replication of results In Section 4, we provide the detailed parameters used for obtaining the results of the four numerical examples. In addition, we include the ABAQUS® user subroutine UMAT as supplementary material, which can be used to reproduce results presented in the paper.

Appendix A. Illustration of the energy control approach

Let us consider a ground structure-based elastic formulation (Bendsøe and Sigmund 2003; Christensen and Klarbring 2009; Sanders et al. 2017), in which (43) can be written as:

$$\begin{aligned} &\max_{\boldsymbol{x}} \quad U(\boldsymbol{x}, \boldsymbol{u}(\boldsymbol{x})) \\ &\text{s.t.} \quad \sum_{e=1}^{n} L_e^T x_e - V_{\max} \le 0 \\ &\quad x_e^{\min} \le x_e \le x_e^{\max}, e = 1, \ldots, n \\ &\text{with} \begin{cases} \boldsymbol{T}(\boldsymbol{x}, \boldsymbol{u}(\boldsymbol{x})) = \chi(\boldsymbol{x}, \boldsymbol{u}(\boldsymbol{x})) \boldsymbol{f}_0 \\ \boldsymbol{f}_0^T \boldsymbol{u}(\boldsymbol{x}) = 2C_0 \end{cases} \end{aligned} \tag{56}$$

The vector $\boldsymbol{x}$ is a vector of design variables, with component x_e being the cross-sectional area of truss member e—it is subjected to lower bound $x_e^{\min}$ and upper bound $x_e^{\max}$. In addition, n is the number of truss members in the ground structure, L_e is the length of truss member e, $V_{\max}$ is the upper bound on the total volume, and $\boldsymbol{u}(\boldsymbol{x})$ is the displacement vector. For illustrative purpose, we assume the particular case of linear elasticity. In the following, we solve a simple three-bar truss example to explain how to estimate a proper value for the prescribed energy C_0 and demonstrate that C_0 remains constant at each design iteration during the entire optimization process.

The three-bar example shown in Fig. 18(a) is made of a linear elastic material with the Young's modulus E = 200 GPa. The structure has two degree of freedoms (dofs), and two reference forces are applied at each dof, respectively. The magnitudes of the two reference forces are $f_{01} = 40$ N and $f_{02} = 80$ N. The displacements at each of the two dofs are u_1 and u_2.

Let us assume that the designer suggests that the magnitudes of initial displacements at each of dofs are the same, i.e., $u_1 = u_2 = 10^{-5}$ m. Based on this assumption, we estimate C_0 as:

$$C_0 = C_{01} + C_{02} = \frac{1}{2} f_{01} u_1 + \frac{1}{2} f_{02} u_2 = 6 \times 10^{-4}\ \mathrm{N \cdot m} \tag{57}$$

This three-bar optimization problem converges with 72 iterations. As an example, we plot the topologies at optimization iteration #1, #35, and #72 in Fig. 18(b), (c), and (d), respectively. Table 11 shows the prescribed energy C_0 at each optimization design iteration, which is composed of the energy C_{01} and C_{02} at each dof, respectively. As expected, C_0 remains a constant in each optimization iteration. The data in Table 11 can be visualized in Fig. 19(a) and (b), which illustrate the energy control approach during the optimization process.

Appendix B. Estimating the limit value of the prescribed energy C_0

Here, we provide a rational approach to estimate the limit value of the prescribed energy C_0 for a design optimization problem given a fixed volume constraint. This approach includes two phases as follows:

Phase #1: Calculate an initial guess of the C_0^0 based on an approximated displacement vector $\boldsymbol{u}$

$$C_0^0 = \frac{1}{2} \boldsymbol{f}_0^T \boldsymbol{u} \tag{58}$$

Phase #2: Estimate the limit value of the prescribed energy $\left(C_0^i\right)_{\lim}$ for the given optimized topology corresponding to the prescribed energy C_0^i.

- At step i (i = 0, 1, 2…), perform FEM analysis of the optimized topology obtained with C_0^i, and plot the curve that represents the relationship between the prescribed energy C_0 and the reaction load factor χ.

- Select two points on the curve (i.e., C_0 versus χ). One of the two points is $\left[C_0^i,\ \chi^i\right]$, and the other point $\left[\left(C_0^i\right)_k,\ \left(\chi^i\right)_k\right]$ is obtained iteratively such that:

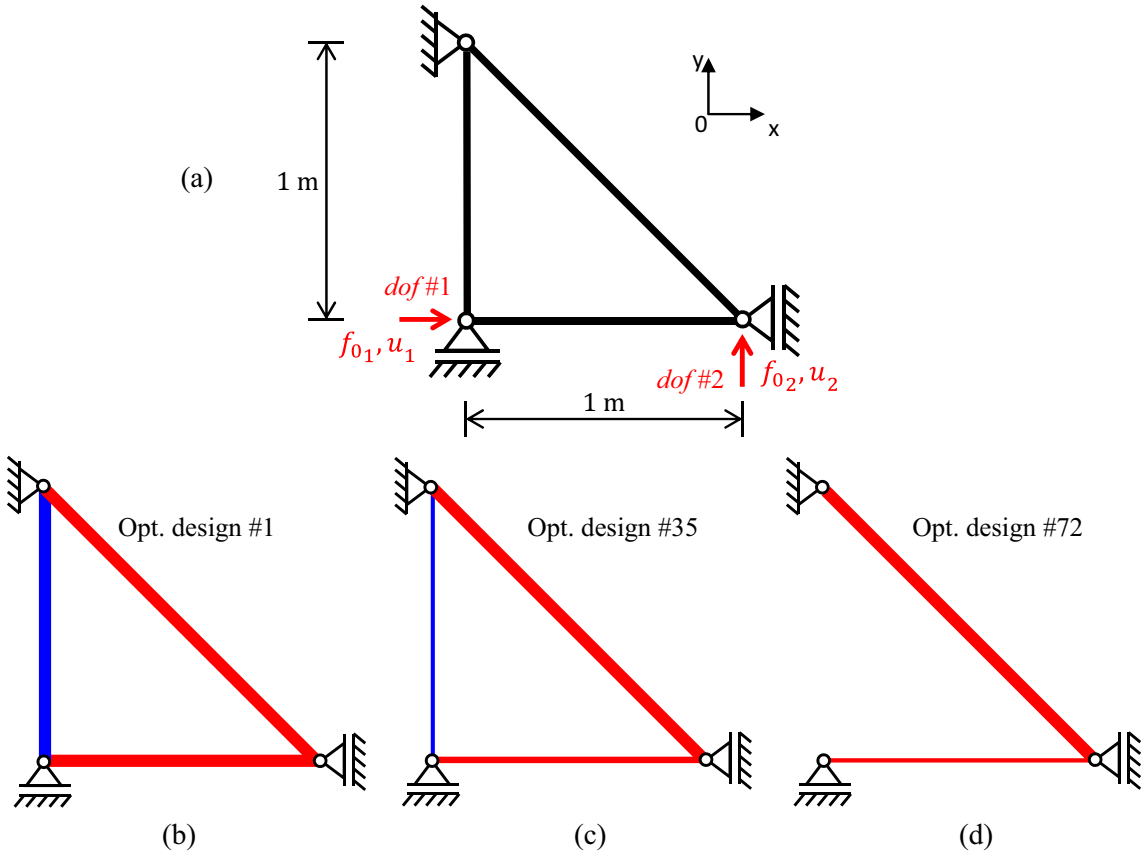

Fig. 18 The three-bar truss example. **a** Design domain and boundary conditions. **b**, **c**, and **d** are the topologies at optimization iteration #1, #35, and #72, respectively. Blue bars are in tension and red bars are in compression

$$\frac{(\chi^i)_k-(\chi^i)_{k-1}}{(C_0^i)_k-(C_0^i)_{k-1}}\leq\beta K_0 \tag{59}$$

where K_0 is the slope of the curve as C_0 is close to zero, and β is a small ratio (e.g., 4×10^{-2} as appropriate).

- Based on the two selected points $\left[C_0^i,\ \chi^i\right]$ and $\left[(C_0^i)_k,\ (\chi^i)_k\right]$, build an asymptotic function with the functional format as follows:

$$\chi(C_0)=\frac{aC_0}{b+C_0} \tag{60}$$

- Calculate the limit value of the prescribed energy $(C_0^i)_{\lim}$ at the current step i as follows:

$$(C_0^i)_{\lim}=b\left(\frac{1}{\sqrt{\alpha}}-1\right) \tag{61}$$

where α is a small ratio (e.g., 2×10^{-2} as appropriate).

Table 11 Calculation of the prescribed energy at each optimization iteration

Optimization Iteration #	u_1 ($\times10^{-5}$m)	u_2 ($\times10^{-5}$m)	$C_{01}=(1/2)f_{01}u_1$ ($\times10^{-5}$N · m)	$C_{02}=(1/2)f_{02}u_2$ ($\times10^{-5}$N · m)	$C_0=C_{01}+C_{02}$ ($\times10^{-5}$N · m)
0	1	1	20	40	60
1	0.2436	1.3782	4.872	55.128	60
35	0.4288	1.2856	8.576	51.424	60
72	0.6	1.2	12	48	60

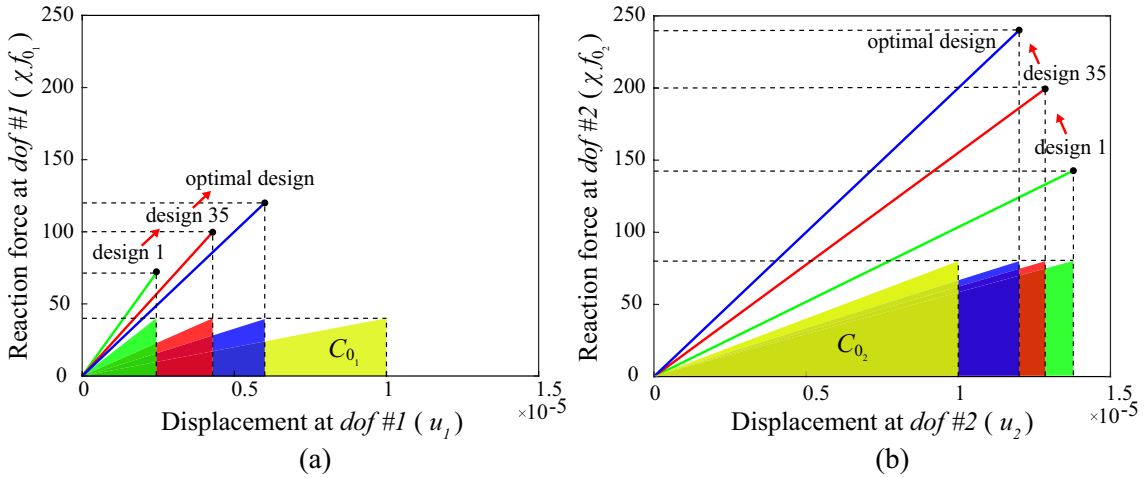

Fig. 19 Displacement versus reaction force diagrams at (**a**) dof #1 and (**b**) dof #2, respectively. The shaded area represents prescribed energy at optimization iteration #0 (yellow), #1 (green), #35 (red), and #72 (blue), i.e., optimal design

- Proceed to step $i+1$. Stop, if the following criterion is satisfied

$$\frac{\left|\left(C_0^{i+1}\right)_{\text{lim}}-\left(C_0^{i}\right)_{\text{lim}}\right|}{\left(C_0^{i}\right)_{\text{lim}}}\leq 5\% \tag{62}$$

- Then, $\left(C_0^{i+1}\right)_{\text{lim}}$ is the estimated limit value of the prescribed energy for the given a fixed volume constraint.

For example, we investigate the limit value of the prescribed energy for the clamped design optimization problem in Section 4.2 using the approach mentioned above. In Fig. 20(a), the red curve represents the structural response of the optimized topology obtained with $C_0^0 = 0.013$ MJ (see Fig. 20(b)), and the black curve is an asymptotic approximation based on (60). From (61), we can obtain the limit prescribed energy for this topology (Fig. 20(b)) as

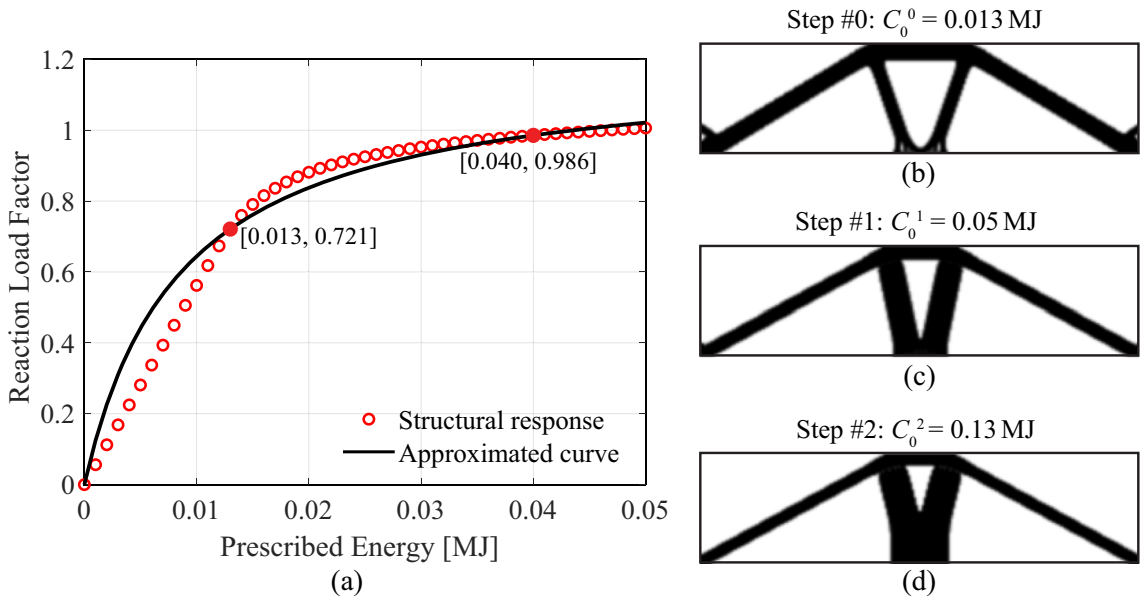

Fig. 20 (**a**) Structural response and its approximation for the optimized topology in (**b**) with $C_0^0 = 0.013$ MJ. (**c**) Optimized topology with $C_0^1 = 0.05$ MJ. (**d**) Optimized topology with $C_0^2 = 0.13$ MJ

$\left(C_0^0\right)_{\lim} = 0.05$ MJ. With this value of the prescribed energy, the corresponding optimized topology is shown in Fig. 20(c). Similarly, we estimate the limit value of the prescribed energy for this topology as $\left(C_0^1\right)_{\lim} = 0.13$ MJ. We repeat the procedure until (62) is satisfied, and then, the limit value of the prescribed energy for this clamped problem is obtained as $\left(C_0^2\right)_{\lim} = 0.134$ MJ. As the prescribed energy increases, the corresponding topologies shown in Fig. 20(b), (c), and (d) are not changing. Instead, we note that the shape of those topologies is different.

Appendix C. Relationship between the increment of principal stress on the strength surface and the increment of principal strain

A reference principal strain tensor of the deformation at a material point can be written as:

$$\left[\varepsilon^{\text{ref}}\right] = \begin{bmatrix} \varepsilon_1^{\text{ref}} & 0 & 0 \\ 0 & \varepsilon_2^{\text{ref}} & 0 \\ 0 & 0 & \varepsilon_3^{\text{ref}} \end{bmatrix} \tag{63}$$

and the principal strain tensor controlled by a positive scaling factor ξ is denoted by:

$$[\varepsilon] = \xi\left[\varepsilon^{\text{ref}}\right] \tag{64}$$

Then, the first invariant of the principal strain tensor is:

$$J_1 = \xi J_1^{\text{ref}} \tag{65}$$

By making reference to (1), we can calculate the principal stress components as:

$$\sigma_i = \xi\left(\lambda\, J_1^{\text{ref}} + 2\,\mu\,\varepsilon_i^{\text{ref}}\right), \quad i = 1,2,3 \tag{66}$$

where λ and μ can be obtained from (4), (9), and (10) considering the Drucker–Prager criterion.

Next, by taking the derivatives of the principal stresses components with respect to the scaling factor ξ, we obtain that:

$$\frac{d\sigma_i}{d\xi} = \left(\lambda + \xi\frac{d\lambda}{d\xi}\right) J_1^{\text{ref}} + 2\left(\mu + \xi\frac{d\mu}{d\xi}\right)\varepsilon_i^{\text{ref}} \tag{67}$$

We then check that the terms in parentheses in (67) are independent of the scaling factor ξ, i.e.,

$$\lambda + \xi\frac{d\lambda}{d\xi} = \frac{\left(1-6\beta^2\right) J_1^{\text{ref}}\sqrt{J_2^{\text{ref}}} - \beta\left(6J_2^{\text{ref}} - J_1^{\text{ref}\,2}\right)}{3J_1^{\text{ref}}\sqrt{J_2^{\text{ref}}}\left[6\beta^2(1+\upsilon)+1-2\upsilon\right]}E \tag{68}$$

and

$$\mu + \xi\frac{d\mu}{d\xi} = \frac{6\beta\sqrt{J_2^{\text{ref}}} - J_1^{\text{ref}}}{2\sqrt{J_2^{\text{ref}}}\left[6\beta^2(1+\upsilon)+1-2\upsilon\right]}\beta E \tag{69}$$

Therefore, we conclude that the increment of principal stress on the Drucker–Prager strength surface is constant for each reference strain tensor with respect to the increment of the principal strain.

Appendix D. Solving the nonlinear state equations: Newton's method with line search

We solve (44) using Newton's method with a backtracking line search strategy. We start with the Lagrangian function.

$$\mathcal{L}(\boldsymbol{u}, \chi) = U(\boldsymbol{u}) + \widetilde{\chi}\left(2C_0 - \boldsymbol{f}_0^T\boldsymbol{u}\right) \tag{70}$$

where $\widetilde{\chi}$ is the Lagrangian multiplier, which is also the reaction load factor in (43). According to the KKT optimality conditions, we readily obtain:

$$\begin{cases} \dfrac{\partial\mathcal{L}}{\partial\boldsymbol{u}}\left(\boldsymbol{u}^*, \chi^*\right) = \nabla U\left(\boldsymbol{u}^*\right) - \chi^*\boldsymbol{f}_0 = 0 \\ \dfrac{\partial\mathcal{L}}{\partial\chi}\left(\boldsymbol{u}^*, \chi^*\right) = 2C_0 - \boldsymbol{f}_0^T\boldsymbol{u}^* = 0 \end{cases} \tag{71}$$

At iteration k, we interpret the Newton step $\Delta\boldsymbol{u}_k$, and the associated multiplier χ_{k+1}, as the solutions of a linearized approximation of the optimality conditions in (71). We substitute $\boldsymbol{u}_k + \Delta\boldsymbol{u}_k$ for $\boldsymbol{u}^*$ and χ_{k+1} for χ^*, and replace the gradient by its linearized approximation near $\boldsymbol{u}_k$, to obtain the equations:

$$\begin{cases} \nabla U(\boldsymbol{u}_k + \Delta\boldsymbol{u}_k) - \chi_{k+1}\boldsymbol{f}_0 \approx \nabla U(\boldsymbol{u}_k) + \nabla\nabla^T U(\boldsymbol{u}_k)\Delta\boldsymbol{u}_k - \chi_{k+1}\boldsymbol{f}_0 = 0 \\ 2C_0 - \boldsymbol{f}_0^T\left(\boldsymbol{u}_k + \Delta\boldsymbol{u}_k\right) = 0 \end{cases} \tag{72}$$

Since $\nabla\nabla^T U(\boldsymbol{u}_k) = \boldsymbol{K}(\boldsymbol{u}_k)$ and $\nabla U(\boldsymbol{u}_k) = \boldsymbol{T}(\boldsymbol{u}_k)$, then, (72) becomes:

$$\begin{cases} \boldsymbol{T}(\boldsymbol{u}_k) + \boldsymbol{K}(\boldsymbol{u}_k)\Delta\boldsymbol{u}_k - \chi_{k+1}\boldsymbol{f}_0 = 0 \\ 2C_0 - \boldsymbol{f}_0^T\left(\boldsymbol{u}_k + \Delta\boldsymbol{u}_k\right) = 0 \end{cases} \tag{73}$$

Table 12 Newton's algorithm for solving nonlinear state equations

Algorithm 1: Newton's method for solving the nonlinear equations

Input: $\boldsymbol{\rho}$, C_0, $\boldsymbol{f}_0$, tol.

Output: Solution f and $\boldsymbol{u}$;

1: $\boldsymbol{u}_0' \coloneqq$ zeros(size($\boldsymbol{f}_0$)); $\boldsymbol{K}_0 \leftarrow$Global stiffness matrix [$\boldsymbol{\rho}$, $\boldsymbol{u}_0'$]; $\boldsymbol{u}_0'' \coloneqq \boldsymbol{K}_0 \backslash \boldsymbol{f}_0$;

2: $\boldsymbol{u}_0 \coloneqq \frac{2C_0 \boldsymbol{u}_0''}{\boldsymbol{f}_0{}^T \boldsymbol{u}_0''}$

3: **for** $k = 0, 1, \ldots,$ until convergence

4: $\boldsymbol{T}_k \leftarrow$ Internal force vector [$\boldsymbol{\rho}$, $\boldsymbol{u}_k$];

5: $\boldsymbol{K}_k \leftarrow$ Global stiffness matrix [$\boldsymbol{\rho}$, $\boldsymbol{u}_k$]; $t_{TK} \coloneqq 10^{-8} \times \text{mean}(\text{diag}(\boldsymbol{K}_k))$;

6: $\boldsymbol{K}_k \coloneqq \boldsymbol{K}_k + t_{TK} \times \text{sparse}(\text{identity}(\text{size}(\boldsymbol{K}_k))$;

7: $\Delta \boldsymbol{u}_k' \coloneqq \boldsymbol{K}_k \backslash \boldsymbol{T}_k$; $\Delta \boldsymbol{u}_k'' \coloneqq \boldsymbol{K}_k \backslash \boldsymbol{f}_0$;

8: $\chi_{k+1} \coloneqq \frac{\boldsymbol{f}_0{}^T \Delta \boldsymbol{u}_k'}{\boldsymbol{f}_0{}^T \Delta \boldsymbol{u}_k''}$;

9: $\Delta \boldsymbol{u}_k \coloneqq -\Delta \boldsymbol{u}_k' + \chi_{k+1} \Delta \boldsymbol{u}_k''$;

10: Find a step size α_k by an inexact line search (Ascher and Greif 2011);

11: $\boldsymbol{u}_{k+1} \coloneqq \boldsymbol{u}_k + \alpha_k \Delta \boldsymbol{u}_k$;

12: **if** $\frac{\|\Delta \boldsymbol{u}_k\|}{1+\|\boldsymbol{u}_{k+1}\|} < tol$ or $\frac{\|\boldsymbol{T}_k - \chi_k \boldsymbol{f}_0\|}{\|\boldsymbol{f}_0\|} < tol$ **then break**;

13: **end if**

14: **end for**

15: $\chi \coloneqq \chi_{k+1}$; $\boldsymbol{u} \coloneqq \boldsymbol{u}_{k+1}$;

Solving for $\Delta \boldsymbol{u}_k$ using the first equation in the system (73), we obtain:

$$\Delta \boldsymbol{u}_k = \boldsymbol{K}^{-1}(\boldsymbol{u}_k)\left[-\boldsymbol{T}(\boldsymbol{u}_k) + \chi_{k+1} \boldsymbol{f}_0\right] \tag{74}$$

By means of the equality $\boldsymbol{f}_0^T \boldsymbol{u}_k = 2C_0$, the second equation in the system (73) becomes:

$$\boldsymbol{f}_0^T \Delta \boldsymbol{u}_k = 0 \tag{75}$$

Substituting (74) into (75), and solving for χ_{k+1}, we obtain:

$$\chi_{k+1} = \frac{\boldsymbol{f}_0^T \Delta \boldsymbol{u}_k'}{\mathbf{f}_0^T \Delta \boldsymbol{u}_k''} \quad , \Delta \boldsymbol{u}_k' = \boldsymbol{K}^{-1}(\boldsymbol{u}_k)\boldsymbol{T}(\boldsymbol{u}_k) \quad , \Delta \boldsymbol{u}_k'' = \boldsymbol{K}^{-1}(\boldsymbol{u}_k)\boldsymbol{f}_0 \tag{76}$$

By substituting the expression of χ_{k+1} in (76) into (74), we finally obtain the expression of the Newton step $\Delta \boldsymbol{u}_k$ as:

$$\Delta \boldsymbol{u}_k = -\Delta \boldsymbol{u}_k' + \chi_{k+1} \Delta \boldsymbol{u}_k'' \tag{77}$$

For the sake of completeness, the detailed algorithm for Newton's method, as employed in the present work, is provided in Table 12. The stiffness matrix might become singular near the limit state which can cause numerical difficulties. To prevent the possibility of a singular stiffness matrix, we add a Tikhonov regularization (Tikhonov and Arsenin 1977; Ramos Jr and Paulino 2016) parameter t_{TK} into the tangent stiffness matrix as shown in lines 5 and 6 of Table 12. Through the testing of the numerical examples, we verify that the Tikhonov regularization technique is effective.

Appendix E. ABAQUS® UMAT subroutine (ESM)

The ABAQUS® user subroutine UMAT for the surrogate nonlinear elastic constitutive model considering the Drucker–Prager criterion is provided as ESM (Electronic Supplementary Material). A representative example of the supplementary material is presented here. For the Abaqus/CAE usage, please follow this sequence: Property module → Material Editor → General → User Material → Mechanical Constants → Input the user-defined material properties in the sequence of Young's modulus, Poisson's ratio, plastic Poisson's ratio, and uniaxial strength stress. Run analysis with the present UMAT subroutine: Analysis → Edit job → General → User subroutine file.

```
c           ABAQUS user subroutine UMAT
c      This user subroutine implements the nonlinear elastic
c      constitutive model considering the Drucker-Prager criterion.
c      Ref: T. Zhao, E. N. Lages, A. S. Ramos Jr. and G. H. Paulino,
c           'Topology Optimization Considering Drucker-Prager Criterion
c           Using a Surrogate Nonlinear Elastic Constitutive Model'.
c           Structural and Multidisciplinary Optimization
c
       subroutine umat (stress, statev, ddsdde, sse, spd, scd,
     & rpl, ddsddt, drplde, drpldt, stran, dstran, time, dtime,
     & temp, dtemp, predef, dpred, material, ndi, nshr, ntens,
     & nstatv, props, nprops, coords, drot, pnewdt, celent,
     & dfgrd0, dfgrd1, noel, npt, layer, kspt, kstep, kinc)
c
       include 'aba_param.inc'
c
       character*8 material
c
       dimension stress(ntens), statev(nstatv), ddsdde(ntens, ntens),
     & ddsddt(ntens), drplde(ntens), stran(ntens), dstran(ntens),
     & time(2), predef(1), dpred(1), props(nprops), coords(3),
     & drot(3,3), dfgrd0(3,3), dfgrd1(3,3)
c
       double precision vmy, vnu, vnup, vsy, valpha, vks, exx, eyy, gxy,
     & vj1e, vj2e, vphi2, vnum, vden
C
```

Appendix F. Nomenclature

$\boldsymbol{\sigma}$	stress tensor
$\boldsymbol{\varepsilon}$	strain tensor
$\boldsymbol{s}$	deviatoric stress tensor
$\boldsymbol{\varepsilon}_d$	deviatoric strain tensor
$\boldsymbol{I}$	second-order identity tensor
σ_i	principal stress components
ε_i	principal strain components
λ, μ	Lame's parameters
ϕ_1, ϕ_2	functions representing the hardening behavior of the material
$J_1(\boldsymbol{\varepsilon})$	first invariant of the strain tensor
$J_2(\boldsymbol{\varepsilon}_d)$	second invariant of the deviatoric strain tensor
$J_1(\boldsymbol{\sigma})$	first invariant of the stress tensor
$J_2(\boldsymbol{s})$	second invariant of the deviatoric stress tensor
$\boldsymbol{\sigma}^L$	linear elastic limit of the stress tensor
$\boldsymbol{\varepsilon}^L$	linear elastic limit of the strain tensor
$\boldsymbol{\sigma}^N$	nonlinear elastic limit of the stress tensor
$\boldsymbol{\varepsilon}^N$	nonlinear elastic limit of the strain tensor
E	Young's modulus
υ	Poisson's ratio
υ^p	plastic Poisson's ratio
σ_y	uniaxial strength stress
β, k_s	positive constants for an elastic-perfectly-plastic material
φ	strain energy density
φ^L	linear elastic strain energy density
c	Cohesion
ψ	friction angle
η, ζ	parameters defined based on the approximation to the Mohr–Coulomb criterion
σ_c	material compressive strength
σ_t	material tensile strength
U	structural strain energy
C_0	prescribed energy
$\boldsymbol{f}_0$	vector of given applied forces
$\boldsymbol{u}$	nodal displacement vector
$\boldsymbol{\rho}$	vector of element density variables
p	constant penalization parameter
Vol	Fracvolume fraction
R	linear density filter radius
n	number of elements discretizing the design domain
v_e	volume of element e
$V_{\max}$	maximum material volume
$\boldsymbol{T}$	internal force vector
χ	reaction load factor
$\widetilde{\chi}$	Lagrangian multiplier
$\boldsymbol{K}_T$	tangent stiffness matrix
$\Delta\boldsymbol{u}$	Newton step
α	step size by backtracking line search
J	objective function
$\mathcal{L}$	Lagrangian function
w	magnitude of distributed load
$\boldsymbol{x}$	vector of the cross-sectional area for truss members
L_e	length of truss member e
κ	a factor used in the inexact line search approach

References

Alberdi R, Khandelwal K (2017) Topology optimization of pressure dependent elastoplastic energy absorbing structures with material damage constraints. Finite Elem Anal Des 133:42–61

Ascher UM, Greif C (2011) A first course in numerical methods. SIAM, Philadelphia

Bendsøe MP (1989) Optimal shape design as a material distribution problem. Struct Multidiscip Optim 1(4):193–202

Bendsøe MP, Sigmund O (1999) Material interpolation schemes in topology optimization. Arch Appl Mech 69:635–654

Bendsøe MP, Sigmund O (2003) Topology optimization: theory, methods and applications. Springer, Berlin

Bogomolny M, Amir O (2012) Conceptual design of reinforced concrete structures using topology optimization with elastoplastic material modeling. Int J Numer Methods Eng 90(13):1578–1597

Borrvall T, Petersson J (2001) Topology optimization using regularized intermediate density control. Comput Methods Appl Mech Eng 190(37–38):4911–4928

Bourdin B (2001) Filters in topology optimization. Int J Numer Methods Eng 50(9):2143–2158

Boyd S, Vandenberghe L (2004) Convex optimization. Cambridge University Press, Cambridge

Chen WF, Han DJ (1988) Plasticity for structural engineers. Springer-Verlag, New York

Christensen PW, Klarbring A (2009) An introduction to structural optimization. Springer, Linköping

Crisfield MA (1991) Non-linear finite element analysis of solids and structures - volume 1: essentials. John Wiley & Sons

Davidson MW (2010) Robert Hooke: physics, architecture, astronomy, paleontology, biology. Lab Med 41(3):180–182

Drucker DC, Prager W (1952) Soil mechanics and plastic analysis or limit design. Q Appl Math 10(2):157–165

Hencky H (1924) Zur Theorie plastischer Deformationen und der hierdurch. Z Angew Math 4(4):323–334

Hill R (1950) The mathematical theory of plasticity. Oxford University Press, Oxford

Holmes DP (2019) Elasticity and stability of shape shifting structures. Curr Opin Colloid Interface Sci 40:118–137

Hooke R (1678) Lectures De Potentia Restitutiva, or of Spring. Explaining the Power of Springing Bodies. John Martyn, London

Kachanov LM (1971) Foundations of the theory of plasticity. North-Holland Publishing Company, Amsterdam

Klarbring A, Strömberg N (2012) A note on the min-max formulation of stiffness optimization including non-zero prescribed displacements. Struct Multidiscip Optim 45(1):147–149

Lubarda VA (2000) Deformation theory of plasticity revisited. Proc Mont Acad Sci Arts 13:117–143

Lubliner J (1990) Plasticity theory. Macmillan, New York

Luo Y, Kang Z (2012) Topology optimization of continuum structures with Drucker–Prager yield stress constraints. Comput Struct 90–91:65–75

Marsden JE, Hughes TJR (1983) Mathematical foundations of elasticity. Prentice-Hall, Upper Saddle River

Niu F, Xu S, Cheng G (2011) A general formulation of structural topology optimization for maximizing structural stiffness. Struct Multidiscip Optim 43(4):561–572

Ramos Jr AS, Paulino GH (2016) Filtering structures out of ground structures - a discrete filtering tool for structural design optimization. Struct Multidiscip Optim 54(1):95–116

Rozvany GIN (2009) A critical review of established methods of structural topology optimization. Struct Multidiscip Optim 37(3):217–237

Rozvany GIN, Zhou M, Birker T (1992) Generalized shape optimization without homogenization. Struct Optim 4(3–4):250–252

Sanders ED, Ramos Jr AS, Paulino GH (2017) A maximum filter for the ground structure method: an optimization tool to harness multiple structural designs. Eng Struct 151:235–252

Sonato M, Piccolroaz A, Miszuris W, Mishuris G (2015) General transmission conditions for thin elasto-plastic pressure-dependent interphase between dissimilar materials. Int J Solids Struct 64–65:9–21

Souza Neto EA, Perić D, Owen DRJ (2008) Computational methods for plasticity: theory and applications. John Wiley & Sons, Chichester

Swan CC, Kosaka I (1997) Voigt–Reuss topology optimization for structures with nonlinear material behaviors. Int J Numer Methods Eng 40(20):3785–3814

Talischi C, Paulino GH, Pereira A, Menezes IFM (2012) PolyTop: a Matlab implementation of a general topology optimization framework using unstructured polygonal finite element meshes. Struct Multidiscip Optim 45(3):329–357

Tikhonov AN, Arsenin VY (1977) Solutions of ill posed problems. Wiley, New York

Timoshenko SP (1934) Theory of elasticity. McGraw Hill, New York

Univ. of Oxford (2014) Hooke Lecture. https://www.maths.ox.ac.uk/node/893. Accessed 16 July 2020

Zegard T, Paulino GH (2016) Bridging topology optimization and additive manufacturing. Struct Multidiscip Optim 53(1):175–192

Zhao T, Ramos Jr AS, Paulino GH (2019) Material nonlinear topology optimization considering the von Mises criterion through an asymptotic approach: max strain energy and max load factor formulations. Int J Numer Methods Eng 118:804–828